Assessing the Earthquake Recording Capability of an Ocean-bottom Distributed Acoustic Sensing Array in the Sanriku region, Japan

Yaolin Miao[1], Amir Salaree[1], Zack J. Spica[1], Kiwamu Nishida[2], Tomoaki Yamada[2], Masanao Shinohara[2]

[1]Department of Earth and Environmental Sciences, University of Michigan, Ann Arbor, Michigan, USA
[2]Earthquake Research Institute, The University of Tokyo, Tokyo, Japan

Key Points:

- We use similarity-based methods to detect earthquakes with Ocean-bottom Distributed Acoustic Sensing (OBDAS).
- We show that the Sanriku OBDAS can record high-fidelity earthquake waveforms compared with a collocated Ocean-bottom Seismometer (OBS).
- We show that the OBDAS is well capable of recording earthquakes over a broad range of magnitudes, with a large across-channel variability.

This manuscript is a non-peer-reviewed preprint submitted to EarthArXiv. It is also submitted to JGR: Solid Earth for peer-review.

Corresponding author: Yaolin Miao, `yaolinm@umich.edu`

Abstract

Sparse seismic instrumentation in the oceans limits our understanding of the Earth's dynamics. The emerging technology of Distributed Acoustic Sensing (DAS), which can turn existing fiber-optic cable arrays into thousands of seismic sensors, has the potential to fill the data gap. Yet, the power of OBDAS for routine seismic monitoring has to be further explored. In this study, we investigate the recording capability of an ocean-bottom DAS (OBDAS) array in the Sanriku region, Japan. We first compare the manually selected OBDAS recordings with a collocated Ocean-Bottom Seismometer (OBS) and demonstrate that OBDAS could record high-fidelity earthquake waveforms when earthquake amplitude power exceeds the OBDAS noise floor. We then propose two array-based detection methods, Waveform Similarity Search and Spectrum Similarity Search workflows, to detect coherent signals across the OBDAS array. With such workflows, we successfully detect $\approx 80\%$ of cataloged earthquakes within a 100 km radius region, as well as thousands of previously uncataloged local events. At the same time, we also show that the quality and quality of recorded waveforms vary substantially across channels. Our results foreshadow an enticing potential of OBDAS to complement the current sparse underwater seismic network for observational seismology studies.

Plain Language Summary

Distributed Acoustic Sensing (DAS) is a cutting-edge technique that transforms ordinary telecommunication fiber-optic cables into highly sensitive and dense arrays of vibration sensors. Some of these cables are placed underwater, where there is a lack of seismic data, making them potentially valuable for studying areas like subduction zones. However, the reliability and effectiveness of this underwater monitoring remain uncertain. In this study, we sought to evaluate the performance of underwater DAS cables in the Sanriku region, Japan. Over a 12-day period, we analyzed the collected dataset using two specialized detection methods tailored for the dense spatial coverage of DAS. Both methods successfully identified thousands of earthquakes, including events not documented in the local seismic catalog. Our analysis revealed that DAS excels at detecting large-magnitude earthquakes and those occurring in close proximity to the sensors, even capturing subtle signals near the cables. These findings suggest that underwater DAS cables can effectively monitor seismic activity. This implies that DAS technology holds great

potential for enhancing seismic monitoring efforts, providing valuable subsea seismic data to the seismology community.

1 Introduction

Observational seismology heavily relies on collecting high-quality measurements from a wide variety of sources to provide a better understanding of the Earth's dynamics. Due to deployment and maintenance issues and the high cost of conventional ocean-bottom seismometer (OBS) arrays, most seismic sensors are deployed on land, while the oceans – covering more than 70% of the Earth's surface – are only sparsely instrumented (Lay et al., 2009). As a result, many submarine regions of the Earth are critically under-sampled and poorly studied. In addition, the lack of instrumentation in active subduction zones where large earthquakes and tsunamis can occur has often left coastal populations exposed, without a sufficient number of accurate real-time Early Warning systems (EEW; Allen & Melgar, 2019; Chung et al., 2020; Salaree, Spica, & Huang, 2023).

Conventional offshore sensors present important challenges. Among the several types of such instruments, short-period OBS are generally operated for a few hours to a few weeks as they are primarily used in active-source experiments, making them inappropriate for long-duration deployment (Kugler et al., 2007; Mordret et al., 2013). Broadband OBS can be installed for years and are suitable for passive source studies (Shinohara et al., 2004; Dessa et al., 2004; Tonegawa et al., 2013), but the spatial coverage of these instruments is often sparse and their data transfer to observatories is a challenge. For near-shore experiments, some sensor arrays use cables to ensure their real-time and long-term data transmission to landing data centers (e.g., S-net in Japan or the US Ocean Observatories Initiative (OOI); Kanazawa et al., 2016; Delaney & Kelley, 2015). While these types of seafloor seismic observatories are important in mitigating earthquake-related hazards in active subduction zones (Hino et al., 2001; Baba et al., 2005; Farghal et al., 2022), their instrument density is still insufficient to provide detailed interpretation of marine environments and seismic wavefield.

A new complement to traditional instruments is incorporating the existing fiber-optic cables (Howe et al., 2022; Salaree, Howe, et al., 2023) into the current seismic network, with the rapidly evolving technology of Distributed Acoustic Sensing (DAS). DAS is used to repurpose standard fiber-optic cables into arrays of densely spaced (merely meters apart; Grattan and Sun (2000)) seismo-acoustic stations over tens of kilometers. In this fashion, DAS can continuously monitor ground motions of study sites and transmit data in real time. Ocean-bottom DAS (OBDAS) has recently been used to detect and monitor a multitude of physical marine phenomena such as near-coast microseism evolution (Xiao et al., 2022) and surface gravity waves (Williams et al., 2022). It has also been used to image offshore structures with unprecedented resolution (Spica et al., 2020, 2022; Cheng et al., 2021; Williams et al., 2021; Viens, Perton, et al., 2022), detect high-quality acoustic waves (Ugalde et al., 2022; Rivet et al., 2021; Spica et al., 2022; Bouffaut et al., 2022) and observe deep-ocean water mixing processes (Ide et al., 2021). In terms of earthquake seismology, previous studies have shown that OBDAS can record high-fidelity seismic signals from teleseismic, regional, and local, small-magnitude earthquakes (Williams et al., 2019; Lindsey et al., 2019; Sladen et al., 2019; Ugalde et al., 2022; Lior et al., 2021). Ide et al. (2021) recorded tens of earthquakes in Shikoku, Japan using OBDAS while confirming the lower sensitivity of OBDAS to low-frequency contents compared to conventional instruments. The details of DAS monitoring at various frequencies and its limitations have been the subject of recent studies. Viens, Bonilla, et al. (2022) studied the nonlinear amplification behavior in shallow marine sediments in response to earthquake waveforms spanning over a range of magnitudes. Besides, Ide et al. (2021) and Lior et al. (2021) found a relationship between coupling conditions and earthquake recording reliability.

As an emerging technology, the potential of OBDAS for earthquake detection is yet to be further evaluated and discussed. Any such evaluation would involve assessing both the quality of recorded waveforms, as well as the completeness of recorded cataloged events. First, the recording quality of each cable is different from others and its response to ground shaking is complex Lindsey, Rademacher, and Ajo-Franklin (2020). DAS measures the axial deformation with only one component along the entire fiber, meaning its sensitivity to different seismic waves depends on incident angles and cable geometry (Martin et al., 2018; Wang et al., 2018). Also, the ground coupling may not be as good as that of traditional seismometers, and measurement quality varies along the cable (e.g., Lior et al., 2021; Viens, Perton, et al., 2022). As a result, each cable is unique and its quality of seismic recordings should be quantified on a case-by-case basis. On the other hand, research on earthquake detection using OBDAS remains scarce (Lior et al., 2021; Ugalde et al., 2022) and the completeness of the OBDAS-recorded catalogs needs to be examined. Multiple inland DAS studies have discussed several DAS-adapted detection methods and the consequent improvement of existing catalogs. For instance, by applying a modified short-time-average/long-time-average (STA/LTA) method, (Zeng et al., 2022) reported the detection of 32 $M_L < 1.0$ earthquakes with a 7.6 km short fiber-optic cable. Li and Zhan (2018) and Li et al. (2021) showed that Template Matching (TM) techniques can detect local microseismicity far below the noise level in DAS data, allowing for significant improvements to standard earthquake catalogs. Nayak et al. (2021a) used an array-based beamforming method to detect $M \geq 2.4$ local and regional earthquakes in DAS data. More recently, Machine Learning techniques were used to pick P and S-arrivals from earthquakes in DAS recordings (Zhu et al., 2023). While these studies apply different methods based on different features of the study sites, the reliability and performance of such detection methods on the ocean floor, i.e., a high-noise environment, are yet to be explored.

In this study, we investigate the earthquake recording capability of an OBDAS array located in Sanriku, Japan (Fig. 1; see section 2.1). We first quantify the variability and quality of manually picked events across different frequency bands and evaluate the spatial trends. We then use a combination of Waveform Similarity Search (WSS) and Spectrum Similarity Search (SSS) methods to retrieve earthquake waveforms recorded along the 13,722-channel array. These methods are array-based and rely on the application of mixed-sensor waveform similarity. Our results demonstrate the effectiveness of these detection methods in dense arrays. We also compare our results with the events from the Japan Meteorological Agency (JMA) earthquake catalog (*Japan Meteorological Agency website*, n.d.) and show that the Sanriku OBDAS system is able to reliably detect local and regional earthquakes as small as $M_v = 0.7$, and thus greatly increase the number of detections in a 1000-km-radius region.

2 Data

2.1 The Sanriku OBDAS array

The Sanriku fiber-optic cable shown in Fig. 1 was installed in 1996 to sustain an ocean-bottom seismic observatory system (Kanazawa & Hasegawa, 1997). In 2011, the great Tohoku-Oki Earthquake damaged the landing station, and thus the cable system was restored in 2014 accompanied by three 3-component accelerometers, two tsunami-meters, and six dark (i.e., unused) fiber strands (Shinohara et al., 2016). The cable spans over 105 km almost linearly at the average azimuth of ∼ 95°. According to the installation report, the cable is buried under 0.6–0.7 m of sediment until ∼47.7 km from the landing station, at which point a tsunami-meter is installed (pink hexagon in Fig. 1). Several DAS studies have been conducted using this cable (e.g., Shinohara et al., 2019;

Spica et al., 2020, 2022; Shinohara et al., 2022; Fukushima et al., 2022; Viens, Perton, et al., 2022; Viens, Bonilla, et al., 2022; Yin et al., 2023). In this contribution, we use continuous data recorded over 12 days between November 20 and December 2, 2019, using a phase-based AP Sensing N5200A interrogator (Cedilnik et al., 2019). The interrogator was set to record distributed phases over 65 km with a 5-m channel spacing, a 40-m gauge length, and a 500-Hz sampling frequency, resulting in an array of 13,722 channels and a data volume of ∼18 Tb. Each channel and the cabled accelerometers were relocated using the travel times of acoustic waves from airgun shootings (Shinohara et al., 2022). More details about the cable setup and data characteristics are described in Shinohara et al. (2022). In this study, the first OBS and the entire OBDAS array, including the unburied channels, are used to assess the signal quality variability (section 2.3). However, only the buried underwater channels (i.e., channel 300-9600) are used for earthquake detection (sections 3).

The phase data were linearly converted to longitudinal strain (Grattan & Sun, 2000):

$$\varepsilon_{xx} = \frac{\lambda_l}{4\pi\xi n_c GL}\Delta\phi; \tag{1}$$

where ε_{xx} is the principal strain along the x-direction. λ_l, n_c, GL, ξ, and $\Delta\phi$ are laser wavelength in vacuum, the fiber refraction index, gauge length, the fiber optical-elastic coefficient in an isotropic medium (i.e., 0.78), and the measured phase shift, respectively.

2.2 External Waveforms

Our analysis requires earthquake waveforms from inland seismometers in the region (henceforth, external waveforms). The distribution of our selected earthquakes is shown in the supplementary material (Fig. FS1). We collect 10,379 high-SNR ($SNR > 10dB$) S-wave waveforms from 4,585 events on the E-W components (i.e., same azimuth as the Sanriku OBDAS array) from 33 inland Hi-net stations in the nearby region (Fig. FS1). These events are selected to include a wide range of magnitudes, durations, and recorded peak amplitudes.

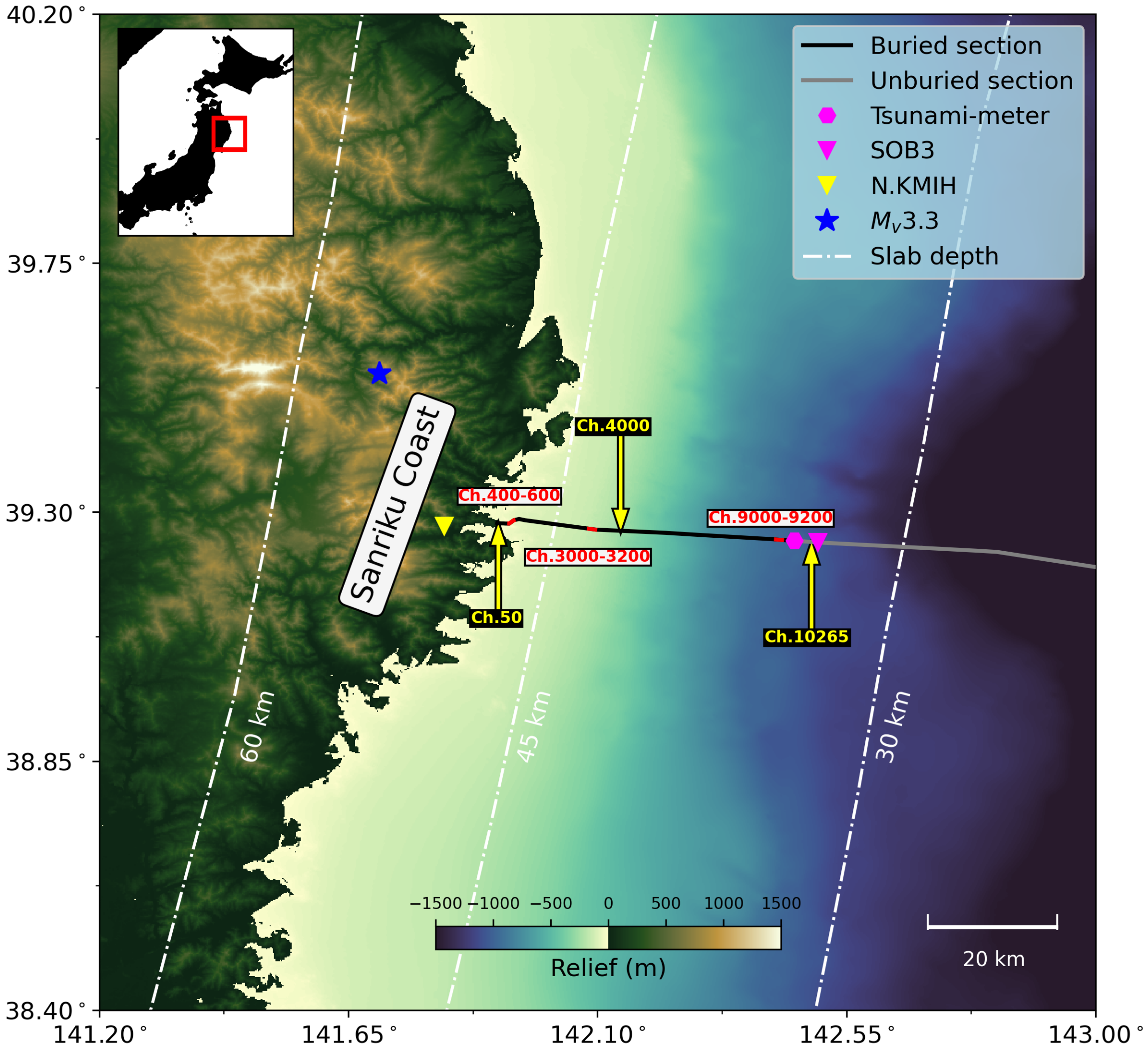

Figure 1: Map of the fiber-optic cable offshore the coast of Sanriku, Japan. The pink and yellow inverse triangles depict a 3-component cabled accelerometer (SOB3) and a short-period seismic station (N.KMIH) used in our analysis, respectively. The pink hexagon is a tsunami-meter. The blue star depicts the hypocenter of an earthquake shown in Fig. 2 (2019-11-23T16:22:03 UTC, 66 km depth, M_v 3.3). The yellow arrows represent the locations of specific channels discussed in the text. Red cable segments highlight the channel sections used in Fig. 9. The red square in the inset map marks the location of the studied region in Japan.

2.3 Preliminary Observations

Below, we analyze the earthquake signals and their recording quality along the Sanriku cable. To this end, we compare the OBDAS records of 35 events to manually inspected, high-quality waveforms at land stations extracted based on arrival times from the JMA catalog. These earthquakes have magnitudes between $1.8 \leq M_v \leq 6.3$ (JMA velocity magnitude scale) and are distributed within 1772 kilometers from the center of the cable at various azimuths (See Fig. FS2 and Table TS1).

2.3.1 Earthquake Signal Variability

Fig. 2 shows the variations in signal-to-noise ratios (SNR) for the set of 35 earthquakes as a function of distance along the fiber (i.e., across different channels) to illustrate waveform variability. SNR is calculated in the time domain in decibels (dB). Signal amplitude is calculated by the average earthquake signal amplitude in a one-second window with the largest average amplitude near its peak amplitude, while the noise amplitude is calculated by the average noise amplitude in a five-second window with the smallest average amplitude, selected before the first seismic arrival. While the different choices of window lengths may result in different numerical values of event SNR, they have a limited impact within the scope of this study because we primarily aim to compare the signal qualities between different events across channels.

In Fig. 2A, we apply a series of narrow-band Gaussian filters and compute the average SNR of filtered waveforms in each band for all earthquakes. The Gaussian filters are designed to be centered in 50 frequencies logarithmically estimated between 0.5 Hz to 20 Hz, with a width of 0.3 Hz. Fig. 2A shows that the largest average SNR (i.e., $\geq$36 dB) is observed between 2-8 Hz in the first $\sim$20km of the cable. Moreover, an average SNR $\gtrsim$20 dB is observed for most of the cable in the 1-8 Hz frequency band, and thus we use this range in the subsequent earthquake detection analyses (section 3).

Fig. 2B shows the SNR variation as a function of distance (i.e., across all the channels) for individual earthquakes in the 1-8 Hz frequency band. The average SNR curves in Fig. 2B (in black and gray for the buried and unburied sections of the cable, respectively) show consistently higher SNR values closer to the shore while generally decreasing moving away from land (Sladen et al., 2019; Williams et al., 2019; Ide et al., 2021). We attribute this to the intrinsic attenuation of laser pulses and their weaker coherence over larger distances (Ide et al., 2021). Although most DAS interrogator manufacturers guarantee nano-strain accuracy over a limited distance (70 km in our case), and noting the rapid evolution of hardware, the current high level of instrumental noise makes

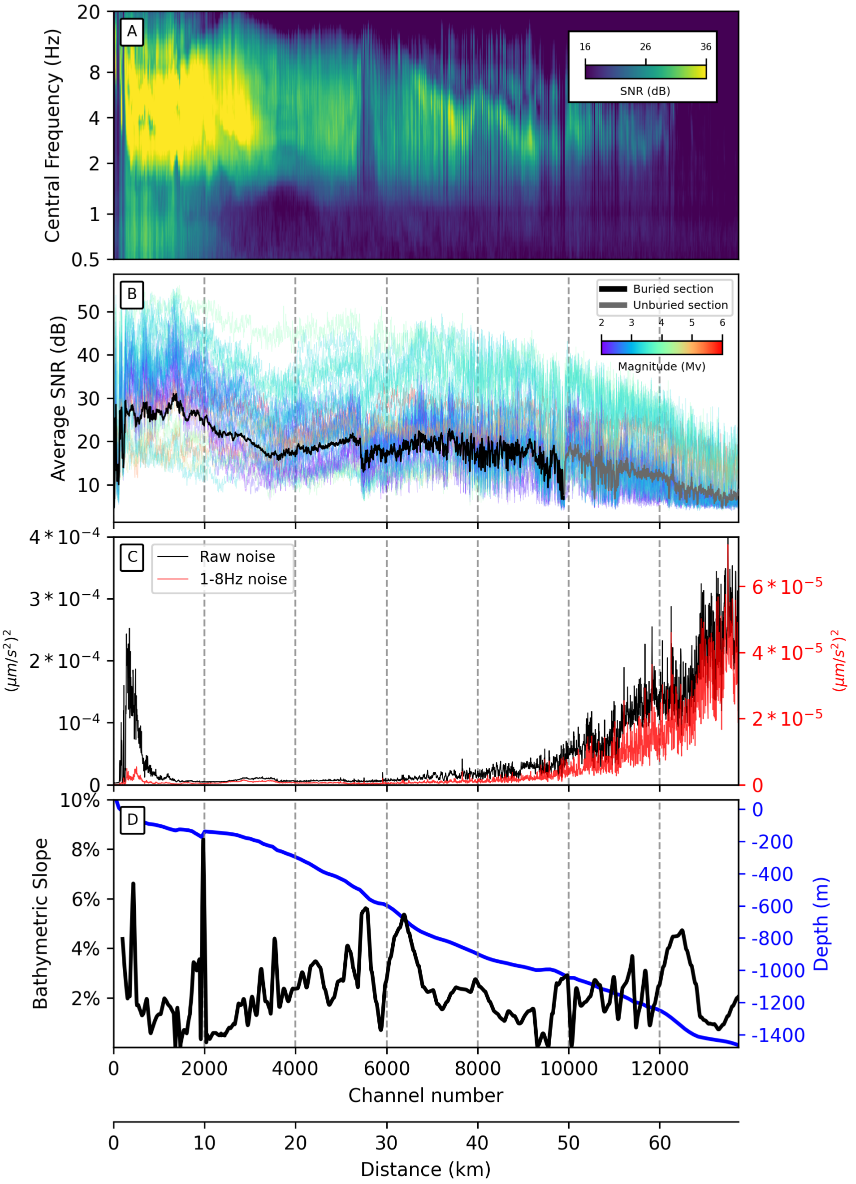

Figure 2: (A) Averaged SNR computed for 35 earthquake waveforms recorded at each channel, bandpass-filtered with a series of narrow-band Gaussian filters, shown over distance from the coast. (B) SNR as a function of the distance from the coast for 35 individual earthquakes in the 1-8 Hz band. The thick, black line in black and gray represents the average of 35 earthquakes. The black and gray subsections represent buried and unburied sections of the cable, respectively. The thinner curves in colors represent the SNR functions of individual earthquakes, with line color scaling with earthquake magnitude. (C) Average noise level of 10-second windows of raw (black) and bandpass filtered between 1 and 8 Hz (red) data. Noise level is calculated in the form of $\Sigma a(t)^2$, where $a(t)$ is OBDAS recordings converted to acceleration (section 2.3.2). (D) Bathymetric slope (in %) and ocean bathymetry along the OBDAS array based on GEBCO and JODC model (*GEBCO 2021 Grid, The General Bathymetric Chart of the Oceans*, 2021; *Japan Oceanographic Data Center 500m Gridded Bathymetry Data*, n.d.).

it increasingly more difficult to detect small transient signals at larger distances from the coast.

While both magnitude and epicentral distance have major impacts on the recorded SNR, we also observe that the distributed properties of the DAS measurements (e.g., spatial variation in physical conditions along the cable) also affect the recorded signal, as demonstrated e.g., by the consistent sharp SNR drops at some subsections of the array for most earthquakes. Firstly, among such properties, the deployment conditions (i.e., buried vs. unburied) of the cable play a major role. As such, the SNR spatial trend shows an abrupt drop at the place where the cable goes from buried to unburied (e.g., near channels 10000; Fig. 2B). Secondly, although the buried section of the cable is expected to provide a relatively uniform cable-ground coupling, the large variations in amplitude across channels can be partially explained by local heterogeneity of seafloor (e.g., van den Ende & Ampuero, 2021). In Sanriku, the local velocity structure has been documented to show rapid changes under the cable (Spica et al., 2020, 2022; Viens, Bonilla, et al., 2022), resulting in local amplification and deamplification of seismic waves, even in the well-coupled regions (Spica et al., 2022; Viens, Bonilla, et al., 2022). Similarly, Viens, Bonilla, et al. (2022) showed that near-coast structures with lower shear wave velocity gradients tend to increase the local amplification of seismic waves. Finally, local bathymetry may also cause discrepancies in waveform quality. Lior et al. (2021) attributed high and low SNR to flat/smooth sections with thicker sediments (e.g., basins), and irregular bathymetry, respectively. Here, we observe a similar relationship between the array SNR and the bathymetric profile. For example, the SNR abruptly decreases near sharp bathymetric features at around channels 2000 and 5600 and tends to increase in regions with gentle slopes (Fig. 2D).

2.3.2 Earthquake Signal Fidelity

In order to quantify the fidelity of Sanriku OBDAS records to seismic signals, we then compare the earthquake signal quality of OBDAS to traditional instruments (i.e., borehole seismometer and OBS). Fig. 3A illustrates the records from an $M_v = 3.3$ (red star in Fig. 1) event and highpass-filtered between 1-8 Hz across channels. The other subpanels in Fig. 3 show the waveforms and spectrograms of the same earthquake from different instruments. For consistency, measurements from different instruments are all converted to acceleration. OBDAS strain-rate recordings are converted by assuming an apparent plane wave velocity of 3500 m/s to retrieve the particle velocity, followed by differentiation to convert to acceleration (e.g., Spica et al., 2020; Shinohara et al., 2022). The Hi-net velocity recordings converted to acceleration via numerical differentiation after removing the instrument response.

As expected, we observe that traditional instruments (Fig. 3B, J) exhibit higher SNR values than OBDAS channels (Wang et al., 2018; Zhan, 2020; Lior et al., 2021; Spica et al., 2020). However, clear P- and S-wave arrivals, as well as possibly surface waves generated by water reverberations (e.g., the waveform highlighted by a red box in Fig. 3F), can be observed at most OBDAS channels, yielding long signal durations on records (Spica et al., 2022). The large amplitude difference between the borehole instrument, KMIH, and the on-land #50 DAS channel (only $\sim$ 57 km apart; Fig. 1) is likely due to site effects (Viens, Bonilla, et al., 2022). Near SOB3 and channel 10,265 (marked by the red triangle in Fig. 3A), we observe a change in the coupling condition (from buried to unburied), leading to more complicated waveforms with higher amplitude codas for the unburied portion (highlighted by a green box in Fig. 3H).

Notwithstanding these intricacies and considering the consistency of DAS waveforms with those from other instruments, we investigate the fidelity of OBDAS waveforms from channel #10,265 to those from SOB3 (see Fig. 1). We first compare the spectral amplitudes of the two instruments for the set of 35 selected earthquakes to examine the fidelity pattern at different frequencies. To do so, we use the SOB3 data and the converted OBDAS recordings in the form of acceleration in 1-minute windows around manually picked S-wave peaks. Fig. 4 compares the two spectra between 0.5 and 20 Hz, revealing spectral matches, i.e., the high fidelity of DAS records within our adopted frequency band ($\sim$1-8 Hz). This is while OBDAS data show higher spectral energies outside this range. For each event, we then find a 10-second window with the highest amplitude power summation ($\Sigma a(t)^2$, with $a(t)$ as a time series of acceleration). Fig. 5A shows earthquake peak amplitude power in the 1-8 Hz band. These results suggest that for the given frequency band, OBDAS measurements are linearly related and are thus unbiased proxies to measure actual ground motion with appropriate calibration coefficients (Yin et al., 2023). Yet, this trend appears valid only for high-SNR events above the OBDAS median noise floor (e.g., Fig. 5B). Finally, while the array is expected to measure seismic phases in the form of axial strain rate along the fiber (Martin et al., 2018), however, arrivals with a wide range of incidence angles are observed from the data. Fig. FS3 shows that OBDAS has similar maximum amplitudes to SOB3 maximum amplitudes at different back-

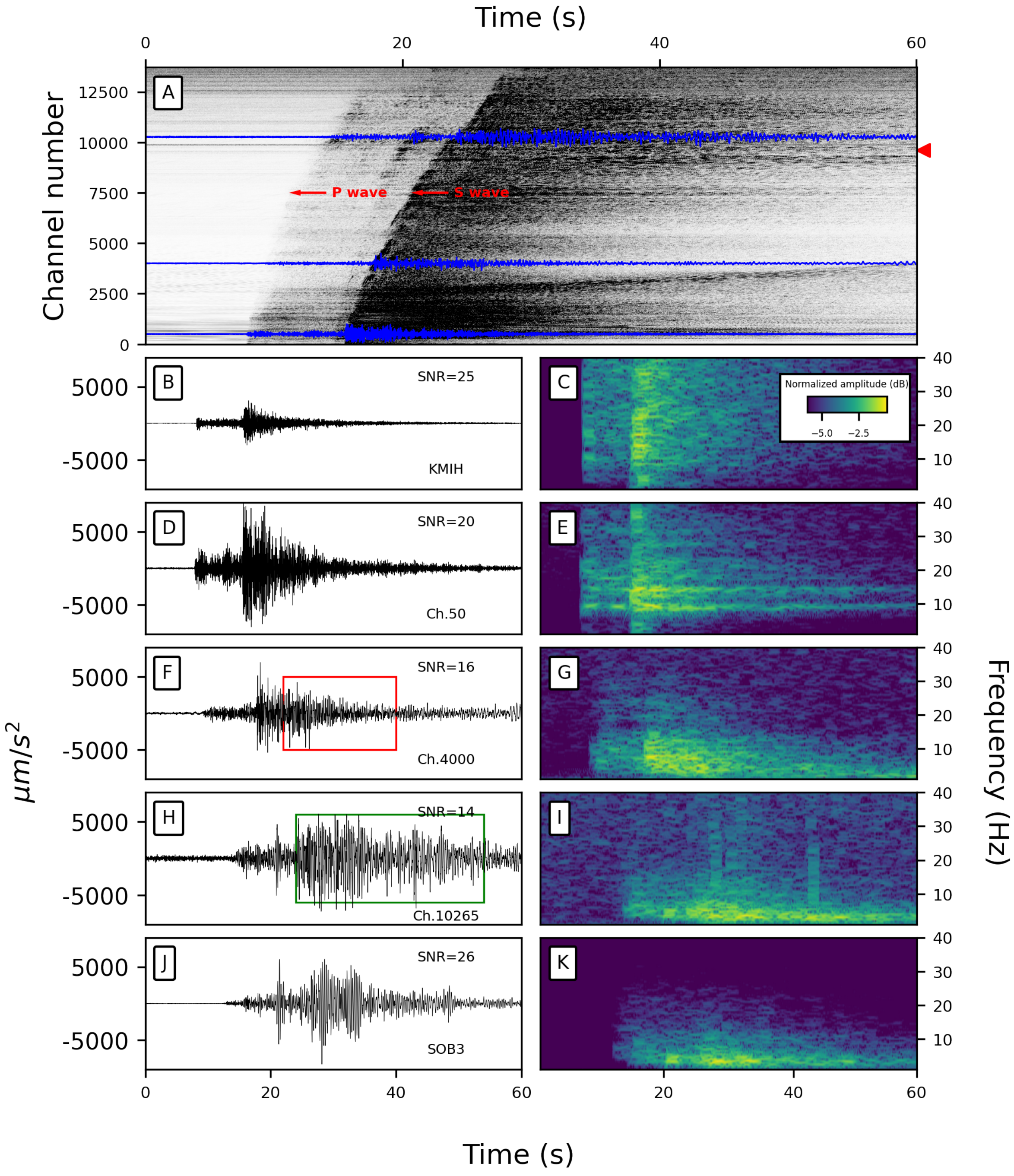

Figure 3: Waveforms for an earthquake (2019-11-23T16:22:03 UTC, 66 km depth, $M_v = 3.3$) highpass-filtered above 1 Hz (epicenter shown by a red star in Fig. 1). (A) OBDAS earthquake wavefield at all OBDAS channels. The three waveforms highlighted in blue are shown in panels D, F, and H, respectively. The red triangle marks the location of the transition from the buried to unburied sections of the cable. Waveform amplitudes are normalized and exaggerated for better visualization. P and S arrivals are labeled with arrows. (B-K) Individual recordings (left) and their normalized spectrograms (right) for different instruments and OBDAS channels. All recordings have a common start time. Channel numbers and station names are included in each panel, along with their respective SNR values. The red box in (F) highlights possible Scholte waves generated by water reverberations at channel 4,000. The green box in panel (H) highlights the extended coda recorded at the unburied channel 10265.

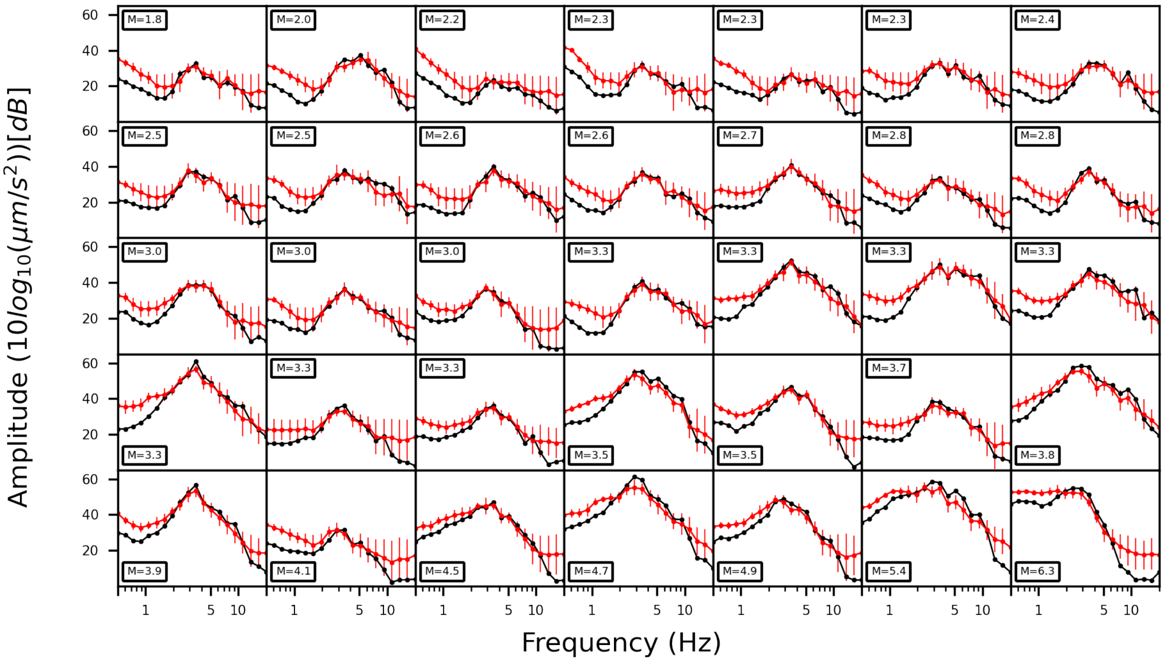

Figure 4: Comparison of the amplitude spectra of the set of 35 earthquake waveforms between channel 10265 of OBDAS (red) and SOB3 (black). The spectra are calculated at 20 frequencies between 0.5 to 20 Hz. 2σ error bars are obtained by spatial averaging over 40 nearby channels (i.e., 200 m).

azimuths. This observation allows us to associate events recorded by the Sanriku OBDAS with a large number of cataloged events, regardless of their incident angles. (Fig. FS3 in supplementary material; Viens, Bonilla, et al., 2022).

3 Methods

We seek OBDAS detection techniques to exploit its dense sampling while minimizing the computational load. Here, we present two array-based detection workflows and discuss their advantages and uncertainties. For subsequent analysis, we only use the buried subsea channels (channel 300-9600); channels 0-300 are excluded because they are on land and are contaminated by a large number of recurring, possibly anthropogenic, short-duration signals (see Fig. FS4).

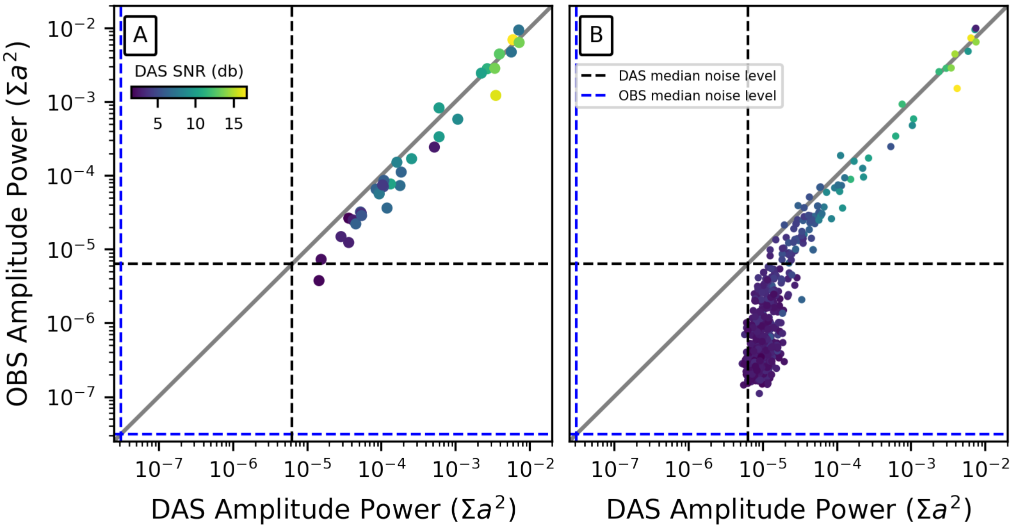

Figure 5: Comparison of seismic signal amplitude power between DAS channel 10265 and SOB3. (A) Comparison for the set of 35 high-quality manually selected earthquakes. (B) Same as (A) but including the newly detected cataloged earthquakes 3. The color scales with the SNR of OBDAS-recorded waveforms. OBDAS and OBS noise level medians (median of amplitude power summation of 10-second noise windows) are shown with the black and blue dashed lines, respectively.

3.0.1 Time Domain Waveform Similarity Search

Our first proposed detection workflow relies on comparing mixed-sensor similarity between OBDAS channels and conventional sensors. Although the mixed-sensor similarity technique has not been extensively used for event detection, the same idea of utilizing similarity between waveforms on DAS and conventional instruments has been proven effective for other purposes such as adjusting DAS-seismometer time move-outs and locating the closest DAS channel to a collocated seismometer, and extracting surface waves in DAS data with seismometers as virtual sources (Lindsey, Yuan, et al., 2020; Nayak et al., 2021b).

We adopt the time domain Waveform Similarity Search (WSS) workflow (Yoon et al., 2015) to detect consistently recorded signals across multiple OBDAS channels considering appropriate move-out. In this approach, we compute the cross-correlation (CC) of OBDAS recordings filtered between 1-8 Hz (see section 2.3.1) with waveforms collected from 33 inland seismometers nearby as external templates (see section 2.1) and then identify the time windows containing the best fits. The cross-correlation is conducted on a one-waveform-to-one-channel basis. This results in a CC function for each OBDAS channel and the corresponding external waveform over time to measure their similarity. A detection is documented at a time window when a CC function exceeds a Median Absolute Deviation (MAD) significance threshold of 9 (Leys et al., 2013; Chamberlain et al., 2018; Li & Zhan, 2018). Simple synthetic tests with boxcar signals are included in the supplementary material (Fig. FS5), proving the efficacy of applying mixed-sensor waveform similarity for detection at various noise levels.

Due to the mixed-sensor nature of the approach and the significant variations in the waveforms across the array (Fig. 3), a single-channel match is not reliable in that, e.g., multiple templates can match a given earthquake or a given template may match a local random vibration at a single channel (Muir et al., 2023). To improve the robustness of detection, we add a spatial consistency criterion, N, as a minimum number of matched channels in 1-s windows (henceforth the N-channel criterion). As multiple waveforms can be matched with the same event, and these external waveforms are not well-aligned. The 1-s window is designed to tolerate the inconsistency of different external waveforms matched at different channels. The N-channel criterion guarantees the spatial coherency of an event along the array while excluding local, sporadic events. As such, we note the trade-off between values of N and the number of detections: while a larger N would enhance the reliability of detections, it may exclude locally recorded, perhaps smaller events, and vice versa. We observe a monotonically decreasing trend in detection numbers against various values of N (Fig. FS6). The quasi-Gaussian distribution of this trend leads to $N = 30$ as a cut-off threshold empirically chosen where the trend falls to $\frac{1}{e}$ of its maximum (Albright et al., 2011). This threshold corresponds to a minimal spatial range of 150 m. Finally, we note that as large earthquakes are often recorded by long subsections of the cable, leading to significant variations in arrival time move-outs, such events are likely to be identified with multiple one-second windows by WSS. Thus, to avoid double counting, we restrict each 14-second window to contain no more than one event. This window length corresponds to the travel time across the 48-km subsection (accounting for the spatial range of 9,600 channels) for detection, assuming an apparent velocity of 3500 m/s. Given that the collected templates are S-waves, we expect that the newly detected coherent events will also be S-waves. However, we note that although these detections share similarities in both time and frequency domains to those of S-waves from earthquakes, their respective sources may or may not always be of tectonic origin.

Fig. 6 shows three examples of WSS-detected earthquakes with various numbers of matched channels. The selective stacking of detecting channels in each case (via including only those with $CC > 0.4$ relative to the channel of highest SNR) in Fig. 6 results in notable improvements to the waveform quality and the emergence of multiple seismic phases. The difference between waveforms by stacking all detected channels and the waveforms with selective stacking further demonstrates that matched waveforms of regional and local events can vary substantially across channels. Besides, WSS detects low-peak amplitude events that are recorded by a short subsection (Fig. 6C, D). These observations further validate the spatial variation of earthquake waveforms (Fig. 3) and illustrate the effectiveness of WSS in capturing subtle local signals over noisy channels.

3.0.2 Spectral Domain Similarity Search

We develop a Spectral domain Similarity Search (SSS) workflow to utilize spectral similarity between OBDAS channels for event detection. SSS uses cross-channel coherence (γ) to identify events that are recorded by individual array subsections. In this approach, coherence is a measure of the similarity between two traces of time series in a predefined frequency band. To account for earthquake waveform variations across subsections of the array (section 2.3.1), we can assume that adjacent channels exhibit greater

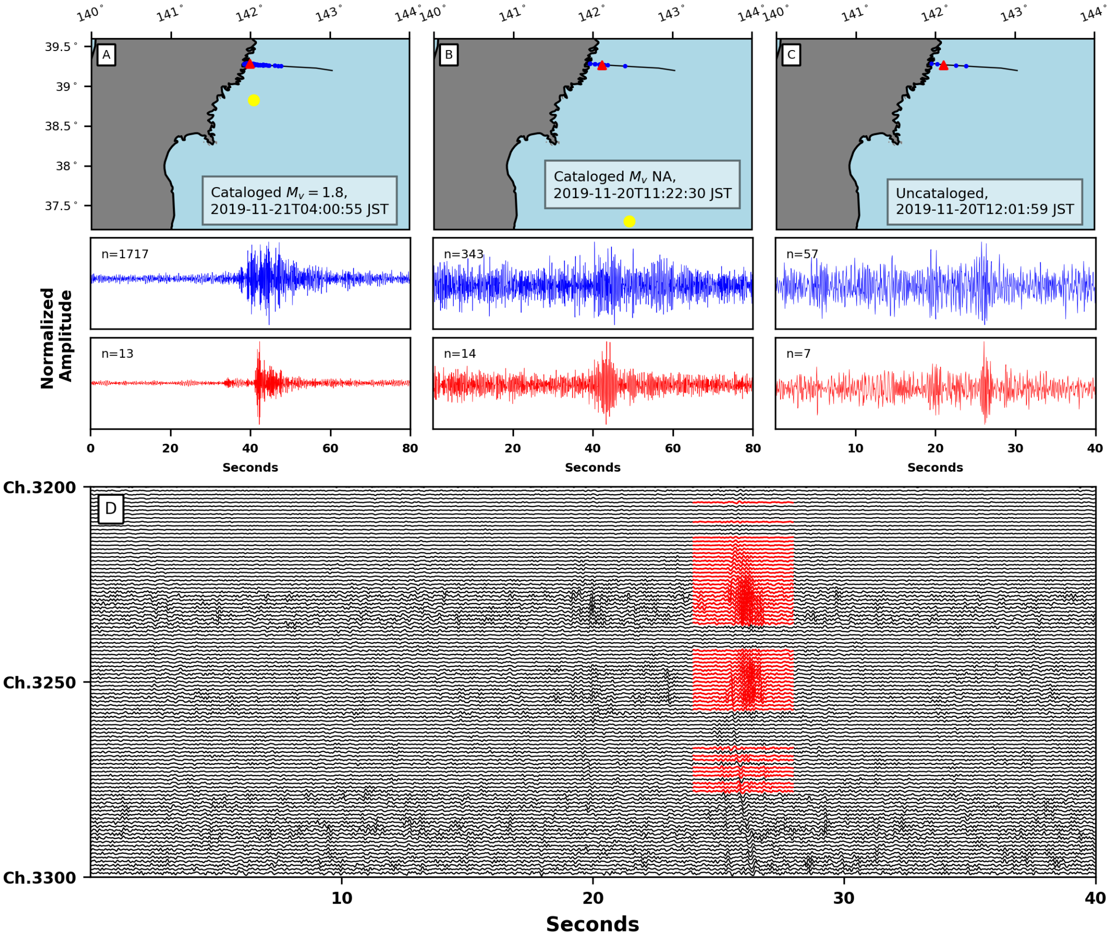

[H]

Figure 6: (A-C) Three examples of WSS detections. For all three subplots in the top panels, the Sanriku DAS array is depicted by a black line. For each event, the matching channels are shown in blue. The red triangles and yellow dots denote the reference channel used for the subsequent stacking and the epicenters of the cataloged events, respectively. The middle panels show the stacked waveforms of all the matching channels (blue) and only those with CC>0.4 with the reference channel (red). The number of used channels for stacking is shown in the top-left corner of each panel. Reference channels are chosen based on waveform SNR. (A) An M1.8 cataloged event (2019-11-21T04:00:55 JST) (B) A catalog event (2019-11-20T11:22:30 JST), whose magnitude is not estimated by JMA. (C) Uncataloged event (2019-11-20T12:01:59 JST) matched with 57 channels. (D) Waveforms of the uncataloged event shown in (C), but across channel 3200 - 3300. Waveforms from matched channels are colored in red.

similarity than those farther apart and thus focus on calculating the median coherence between each channel and its nearby five neighbors (i.e., 25 m). This spatial averaging scheme is adopted to reduce the impact of abrupt high-noise channels. In this fashion, we significantly reduce the computational workload compared to calculating the coherence of all possible channel pairs from the array.

Considering the absence of large regional events during the experiment time interval, we focus primarily on small to moderate magnitudes ($M_v \leq 4.0$). Therefore, we use the average coherence in the 1-8 Hz frequency band for detection (similarly to WSS). This guarantees the inclusion of earthquake corner frequencies in the target spectra based on earthquake source models and scaling laws (Brune, 1970; Geller, 1976). To include relatively complete seismic waveforms of moderate-magnitude earthquakes – e.g., the full waveforms of P, S, S-coda, and surface waves can be as long as 40 s, as demonstrated in Fig. 3) – we use a series of 40-second moving windows with 90% overlap to implement SSS. This overlap rate is selected to allow for arrival time move-outs across channels, as well as to balance the computational workload and window step size. This moving-window technique enables SSS to flag high-coherence time windows with a progression step size of four seconds ($40\text{s} \times (1 - 0.9) = 4$ s). In doing so, based on the larger coherency of earthquake signals compared to ambient noise along the array, for each channel, we define a detection quality threshold, κ, defined by the exceedance from the mean coherence of the same channel as shown in Eq. 2.

$$\kappa = \bar{\gamma_i} + 3\sigma(\gamma_i) \tag{2}$$

In Eq. (2), $\bar{\gamma_i}$ and $\sigma(\gamma_i)$ are the mean and standard deviation of coherence for channel i, respectively. We note that some of the OBDAS channels demonstrate high coherence over half of the windows, presumably because of long-lasting pressure fluctuations in the same frequency band (section 5.3). These channels have large $\bar{\gamma_i}$ and $\sigma\gamma_i$ which may lead to unreliably large κ. To prevent such outliers from reducing detection accuracy, we empirically set a maximum coherence, hence discarding channels with $\bar{\gamma_i} > 0.7$. Moreover, similar to the WSS, high coherence between only one pair of channels is not sufficient to conclude a new event. Consequently, we identify a new event only when more than a certain number of channels exceed their corresponding thresholds over the same time window. For this purpose, we calculate the coherence of all time windows (i.e., $\approx$

$260,000$ 40s-windows over 12 days). The distribution of the number of channels exceeding their coherence thresholds (i.e., high-coherence channels) exhibits a clear normal distribution pattern with a long tail to the right (Fig FS7). The tail is caused by large-magnitude earthquakes with great spatial coherence over all the channels. To minimize the bias of these events on setting channel threshold, we use a MAD threshold and set it as $n = 3 \times MAD = 80$ (red vertical line in Fig. 7C and in FS7).

Following the algorithm described above, traces of continuous time series of all channels are transformed into a two-dimensional coherence matrix. Fig. 7 shows an hour of strain rate records (Fig. 7A) along with a visualization of the corresponding coherence matrix starting on 2019-11-21 at 13:00:00 JST (Fig. 7B). In Fig. 7B, three detected cataloged earthquakes with magnitudes between $M_v = 1.9 - 2.5$ and two uncataloged high-coherence detections are marked. The blue box in Fig. 7B shows a possible event with a lower coherence that does not pass the prescribed thresholds but is otherwise weakly visible and does not appear among the events with a high-coherence channel number as a threshold.

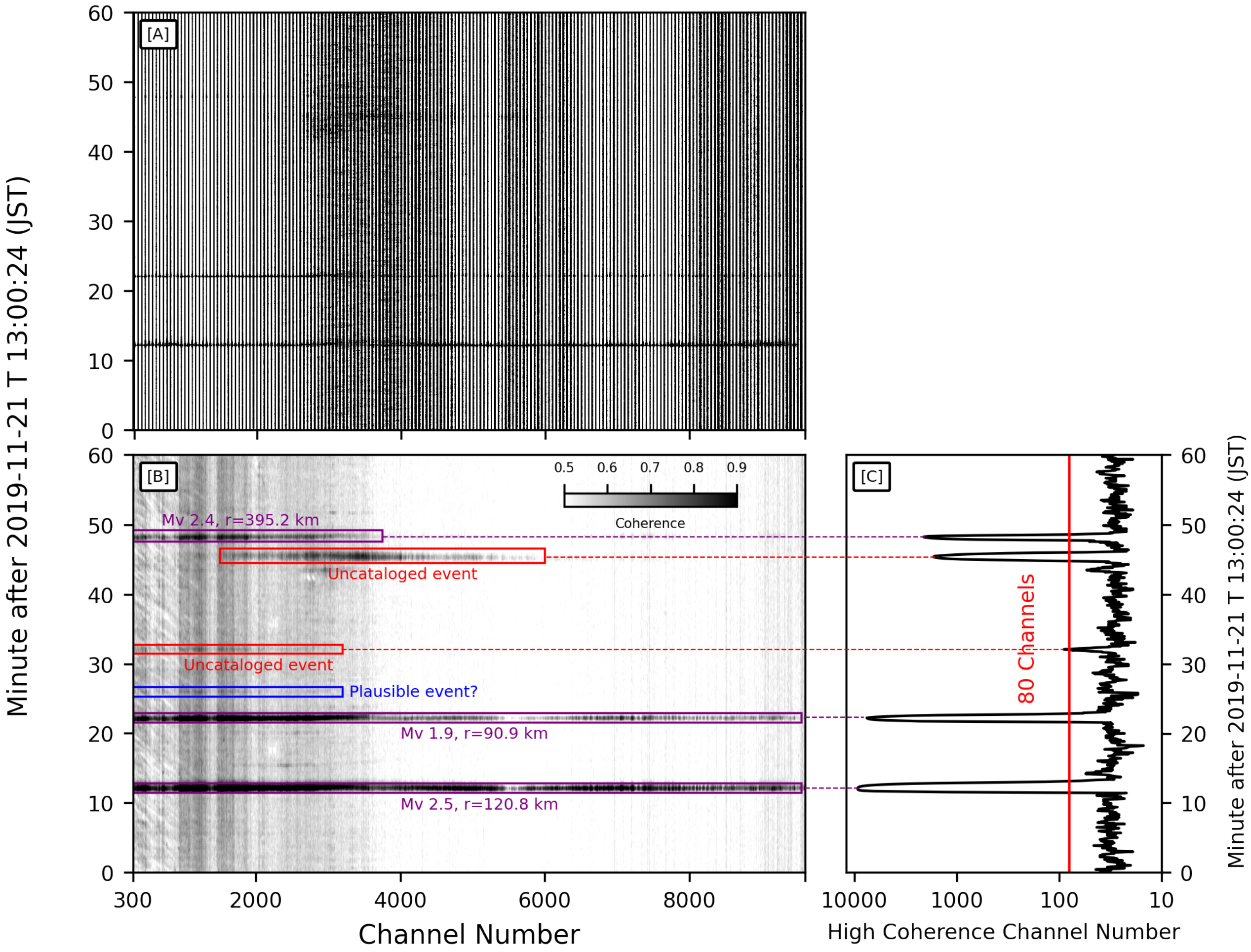

Figure 7: Examples of SSS detections. (A) Time series for an hour of recording starting on 2019-11-21 at 13:00 JST. (B) The coherence matrix of the same period as panel (A). Cataloged and uncataloged detections are highlighted with purple and red boxes, respectively. The blue box marks a plausible event (not detected). (C) Number of high coherence channels as a function of time using the same period as in panel (A-B). The red line corresponds to the 80-high-coherence-channel threshold. Detected events in panel (B) and peaks in panel (C) are connected with dashed lines.

3.1 Associating Detections with Cataloged Events

Due to the small spatial dimension of the detection agents (30-channel and 80-channel thresholds) and considering the quasi-linear geometry of the OBDAS array, locating the detected events would be a challenge (Thurber & Engdahl, 2000). As a result, to assess the quality of our OBDAS detections, we seek to associate them with events in the JMA catalog, mainly relying on computed S-wave arrival times using the 1-D PREM model (PREM Dziewonski & Anderson, 1981). We note that due to the uncertain response of OBDAS (Lindsey et al., 2019) and the complex local velocities in the subducting slab, this approach may lead to arrival time uncertainties reaching a few seconds (Lomax et al., 2009). In fact, perturbation of up to +5% in the PREM velocities for the WSS hypocenters may lead to ~ 5 s within a 1000 km radius of the cable midpoint, i.e., within the 10 s detection window used in WSS for comparison (see FS8). Therefore, a 10-second arrival time window is sufficient to associate WSS events. For SSS detections, however, due to the four-second window-crossings, we use 14s windows in the association process. While the prescribed time windows account for potential uncertainties in travel time, they may also cause mismatching via confusing events with close arrival times, many of which were formerly uncataloged. For instance, such "new" detections (e.g., flagged in Fig. 6 and Fig. 7 and not reported in the JMA catalog), that account for a majority of small events (i.e., 5584 earthquakes with a median magnitude $M_v = 0.7$), may be erroneously categorized as cataloged events upon allowing for time uncertainties. The small magnitudes of such events combined with their relatively large epicentral distances (i.e., a median of $564km$ from the center of the OBDAS array) suggest the abundance of highly attenuated energy at long ray paths. While these earthquakes are unlikely to be detectable at such long distances, they can be a major source of bias.

To remedy this issue, we implement an amplitude threshold to refine the association process further by excluding uncertain earthquakes from the association catalog and hence reducing the likelihood of mismatching. Such amplitude threshold consists of two steps. We first calculate the theoretical amplitude on OBDAS of all earthquakes on the JMA catalog with an empirical scaling relation modified from Yin et al. (2023), for a cataloged earthquake:

$$\log_{10} A^s = 0.69M - 1.588 \log_{10} D + K^s, \tag{3}$$

where A^s represents the theoretical S-wave amplitude on OBDAS of the earthquake;

M represents its cataloged magnitude; D is the hypocentral distance, and K^s is the S-wave correction factor accounting for all local effects. Secondly, we categorize JMA events into two groups, depending on whether their theoretical arrival time range includes any detections among OBDAS events. We label those with a plausible OBDAS counterpart as *plausible*, and others as *unrecorded.* We then analyze the distribution of theoretical amplitudes of *unrecorded* earthquakes and use the 90 percentile of a threshold, assuming any cataloged events with smaller theoretical amplitudes are not sensible of OBDAS and, therefore, excluded from the association process. These JMA events have smaller theoretical OBDAS amplitudes than truly missed events, which suggests they are unlikely to be recorded. They tended to result in incorrect pairings with local uncataloged OBDAS detections with a similar theoretical arrival time if not excluded. All earthquakes share the same correction constant K^s, and its value does not impact the amplitude threshold.

The former further refines the association process by only keeping those events that pass both the arrival time and the amplitude attenuation threshold. It is important to note that excluding certain events does not necessarily and sufficiently imply their absence in OBDAS records. The search for such events requires additional constraints such as location and focal mechanism solution to be used along with theoretical arrival times and amplitudes; whereas such considerations are beyond the scope of this study, their inclusion in future projects may resolve the issue.

4 Results

WSS and SSS detect 10200 and 3591 events from the Sanriku OBDAS data, respectively. These newly detected events are then cross-referenced with the JMA catalog within a 1000 km radius from the midpoint of the OBDAS array. Among the newly detected events using the WSS and SSS methods, 601 and 339 events are associated with cataloged earthquakes, respectively (Tables 1 and 2). Fig. 8 shows the epicenters of detected and undetected cataloged events of both methods.

Table 1: Detection results of WSS

M_v Epicentral Distance	< 2	2 - 3	3 - 4	> 4	Total
0 - 100 km	80.2% (235/293)	100% (22/22)	100% (6/6)	100% (1/1)	82.0% (264/322)
100 - 200 km	57.8% (100/173)	97.2% (35/36)	100% (5/5)	NA(0)	65.4% (140/214)
200 - 500 km	34.3% (36/105)	68.0% (83/122)	85.7% (18/21)	100% (2/2)	55.6% (139/250)
500 - 1000 km	NA(0)	49.2% (29/59)	54.3% (19/35)	90.9% (10/11)	55.2% (58/105)
Total	65.0% (371/571)	70.7% (169/239)	71.6% (48/67)	92.9% (13/14)	67.5% (601/891)

Table 2: Detection results of SSS

M_v Epicentral Distance	< 2	2 - 3	3 - 4	> 4	Total
0 - 100 km	36.2% (106/293)	40.9% (9/22)	83.3% (5/6)	100% (1/1)	37.6% (121/322)
100 - 200 km	28.9% (50/173)	63.9% (23/36)	100% (5/5)	NA(0)	36.4% (78/214)
200 - 500 km	21.0% (22/105)	44.3% (54/122)	85.7% (18/21)	50% (1/2)	38% (95/250)
500 - 1000 km	NA(0)	35.6% (21/59)	54.3% (19/35)	45.5% (5/11)	42.9% (45/105)
Total	31.2% (178/571)	44.8% (107/239)	70.1% (47/67)	50% (7/14)	38.0% (339/891)

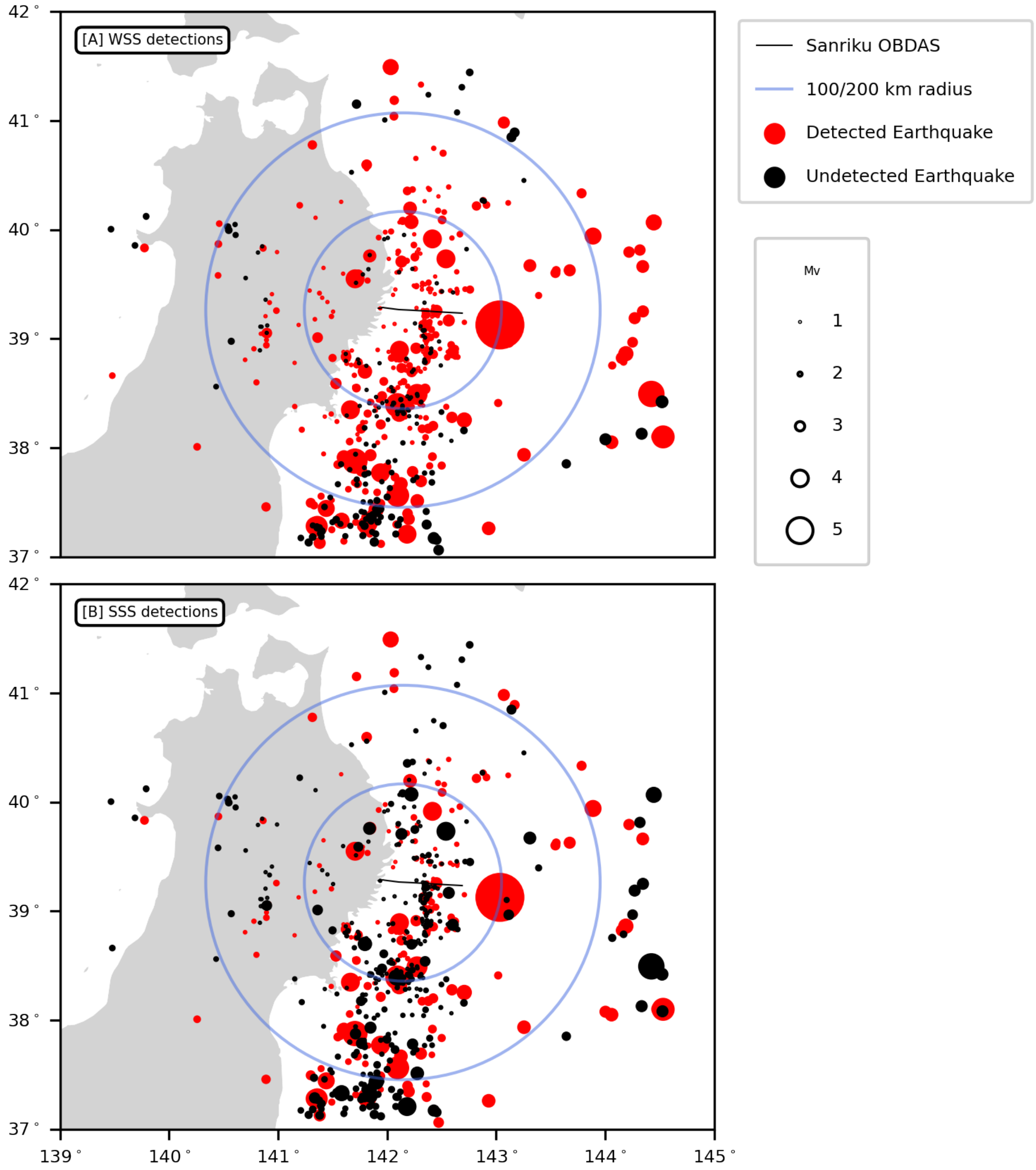

Figure 8: Map of detected (red dots) and undetected (black dots) JMA events using (A) WSS and (B) SSS. Blue circles mark 100 and 200 km radii from the center of the Sanriku OBDAS array. Dot sizes are proportional to earthquake magnitude (M_v). Cataloged events that failed the theoretical amplitude threshold are excluded from the association processes and are not shown.

Fig. 9A, B compares all events and cataloged events detected by the two methods on different OBDAS channels. We observe that although WSS detects three times more events than SSS in total, most of the individual channels have more SSS detections than WSS detections. We find that for all WSS detections, the median number of matched channels is 44 while the median channel number of all SSS detections is 798. Similar observations suggest WSS detects more unique and local events in different subsections, whereas SSS provides more spatially coherent detections. Fig. 9C-E summarizes the magnitude, epicentral distance, and depth distributions of three subsections with large numbers of cataloged detections. For all subsections, the color distribution trend (Fig. 9C-E) shows that at larger epicentral distances, the recorded events are of larger magnitudes, indicating that epicentral distance plays a pivotal role in determining whether an event can be recorded by the OBDAS. However, there is no discernible pattern along depths. Thus, one can conclude that depth is not a factor as critical as epicentral distance in this regard.

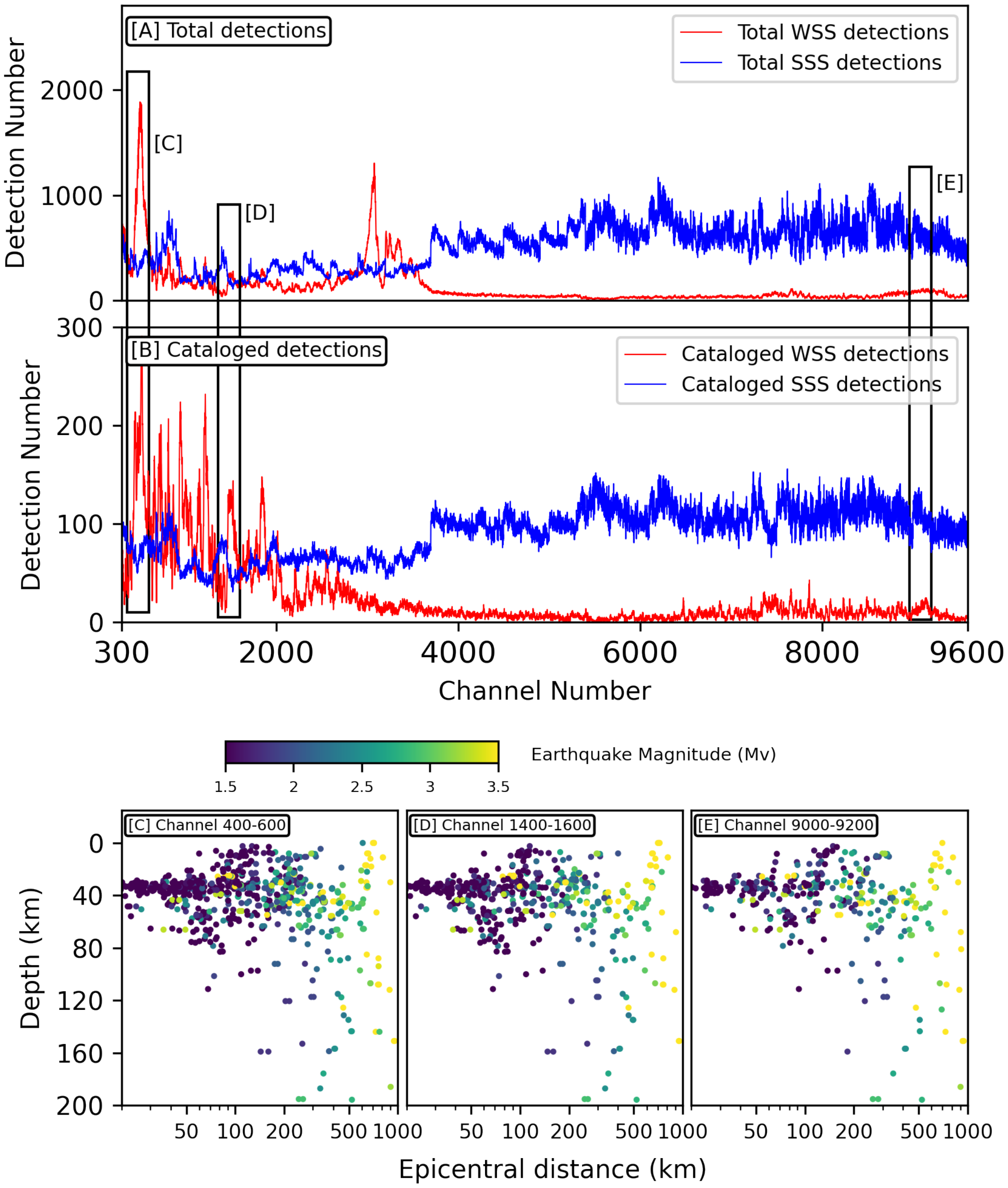

Figure 9: Detection results breakdown by channel. (A) All detections by WSS and SSS on OBDAS channels. (B) Cataloged detections by WSS and SSS. The black boxes highlight three subsections with large numbers of cataloged detections, which are further explained in panel (C-E). (C-E) Epicentral distance and depth distribution of detected earthquakes on channels 400-600, 1400-1600, and 9000-9200, respectively. The locations of these three sections are shown in Fig. 1. Each dot represents one cataloged event detected by the corresponding subsection and its color scales with event magnitude.

5 Discussion

In light of the obtained results, we demonstrate that the proposed methods, WSS and SSS, are capable of detecting seismic events from the ultra-dense DAS array in an underwater environment. It becomes evident that our proposed methods are a good complement to current detection practices with DAS. In this section, we highlight the distinctive detection features and present notable features of our detection results. Another overarching aim of the discussion is to find out whether specific events are missed because of the limitations of the OBDAS system or the limitations of proposed detection workflows. This notion would ultimately contribute to a better understanding of the recording potential of the OBDAS array.

5.1 Double-matched and Masked Events

During the association process, we observe that one cataloged event can sometimes be associated with more than one OBDAS detection. We attribute the *double-matching* to two possible causes: First, as described in the section 3.0.1, the event identification process is based on the arrival times of the matched waveforms across all channels. In the association process, we recognize no more than one event within any 14-second window to constrain multiple-countings. However, the 14-second threshold may not sufficiently compensate for move-outs of events with azimuths in parallel with the array orientation. In this case, *double-matching* is due to the double-counting of one OBDAS detection. An example is presented in Fig. 10. It shows the waveforms of the same earthquake at two ends of the OBDAS array. There are a few seconds of offset between theoretical arrival times with PREM (red curve in Fig. 10B) and realistic arrivals at the end of the array. This observation demonstrates the limitation of relying on a general model for theoretical arrival time calculation and the necessity of allowing an uncertainty window. Meanwhile, the significant variation in arrival times across the array causes this event to be erroneously identified as two different occurrences at two ends of the cable. Consequently, this results in the cataloged counterpart being matched twice. It is also worth highlighting that the waveform on a single channel in the final section of the array is near the noise level (blue trace, $SNR = 4.35$), but shifting and stacking adjacent channels improves the signal quality. This observation further proves the efficacy of mixed-sensor CC for detecting low-SNR events on single channels.

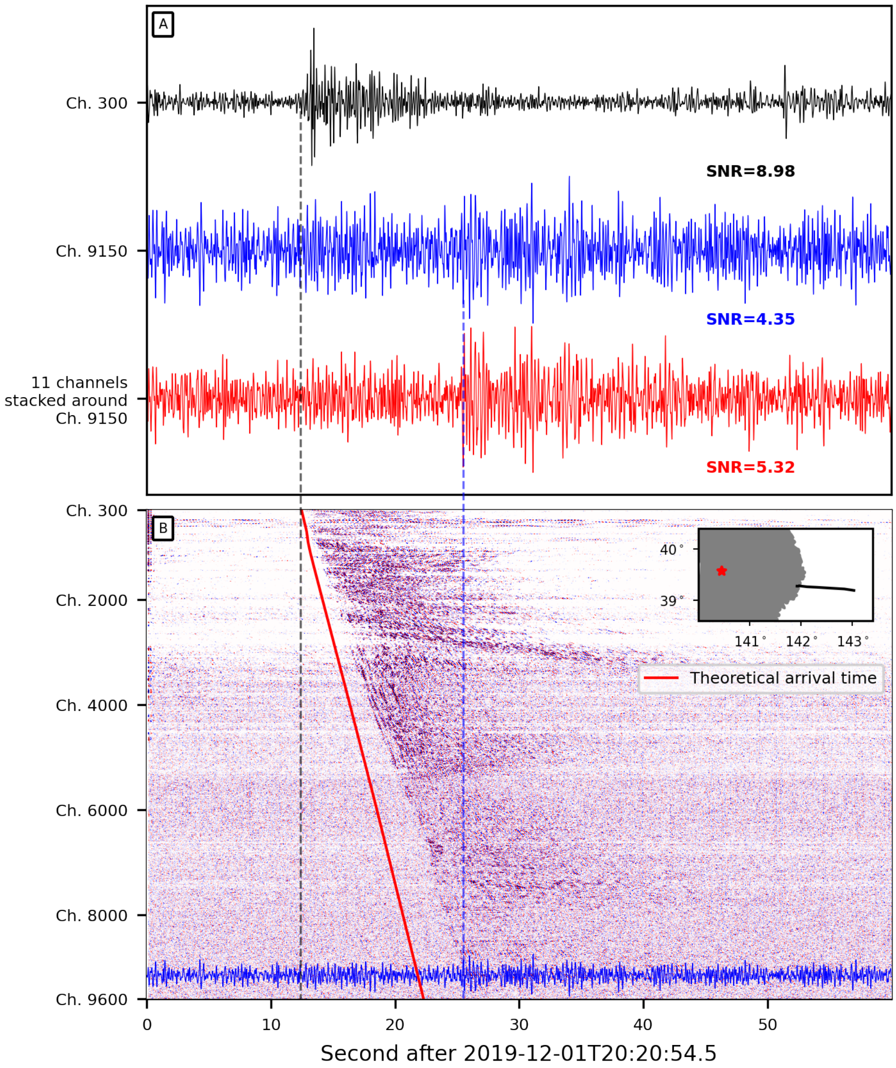

Figure 10: An example with large arrival time move-outs across the array. The cataloged earthquake is $M_v = 1.6$, 150.0 km away from the cable center. (A) Waveforms on channel 300, channel 9150, and a stacked channel are shown in black, blue, and red, respectively. Amplitudes of each trace are normalized. Black, blue, and red waveforms have SNRs of 8.98, 4.35, and 5.32 dB, respectively. (B) Time-series density plot for earthquake waveforms across the array. The red curve represents the theoretical arrival time at each channel based on the PREM model. Amplitudes are exaggerated as in Fig. 3A and the color scale is clipped for a better visualization. The inset map shows the earthquake epicenter with a red star and the location of the Sanriku OBDAS array with a black curve.

Secondly, multiple seismic phases over a short duration on individual channels can result in multiple detections. In some cases, these phases could be the S-wave and surface waves of the same earthquake. In other cases, they could be seismic phases of different events, potentially generating *ghosted* detections. Fig. 11A, B shows possible examples of these two scenarios, respectively. We identify the long tail followed by the impulsive S-wave shown in Fig. 11A as Scholte waves. Similar observations have been noted in a previous study, suggesting they originate from water reverberations (Spica et al., 2022). We follow the similar procedure described in Spica et al. (2022) to examine whether the long tail exhibits a dispersive property. Fig. FS10A-C shows a two-mode dispersion of the phase shown in Fig. 11A. The other example shown in Fig. 11B is characterized by multiple arrivals with high peak amplitudes over a short time ($\approx 20s$), while the waveform on the OBS only indicates a single arrival. We perform a similar dispersion analysis, but no clear dispersion is observed (Fig. FS10D-F). Consequently, we attribute the prolonged phase to the superposition of closely spaced arrivals of a cataloged earthquake followed by possibly small events from the local region near channels 1200-2000. While the physical sources of the phases are speculative, more deterministic approaches such as ray tracing and waveform forward modeling are needed to discriminate the two aforementioned scenarios. Nevertheless, in both instances, the simultaneous presences of multiple seismic phases are identified as two events, leading to the double-matching of the corresponding cataloged event. If those multiple phases originated from different events (i.e., the second scenario), an uncataloged event might be *ghosted* (Fig. 11B).

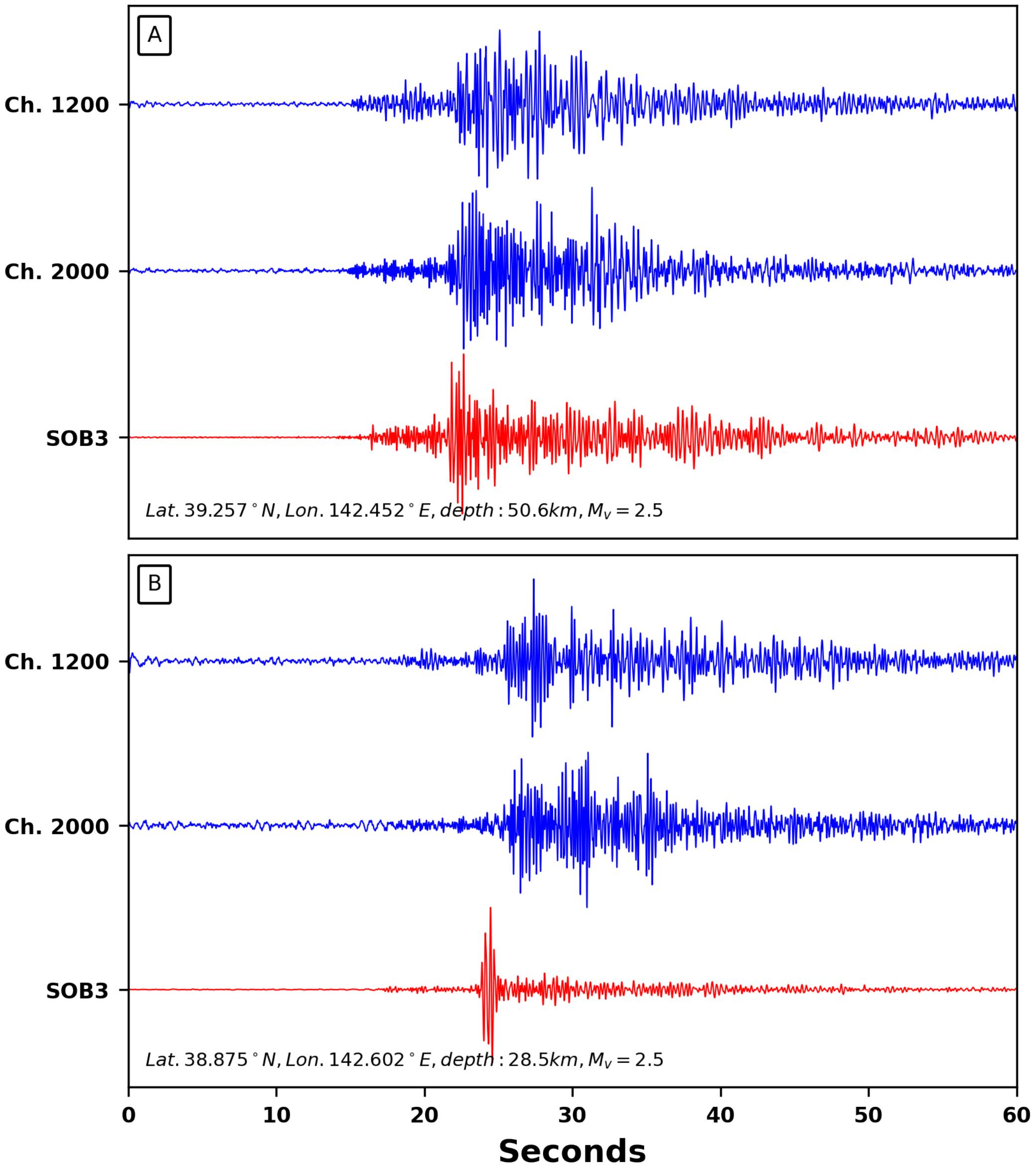

Figure 11: Examples of double-matched events, potentially caused by (A) long-duration Scholte waves, and (B) multiple seismic phases of different events. Waveforms of OBDAS channels (channel 1200 and channel 2000) and SOB3 are shown in blue and red, respectively. Source locations and magnitudes of the associated cataloged earthquakes are shown in the left-bottom corner of each panel.

5.2 Undetected Events

We combine the detection results of both WSS and SSS to scrutinize undetected events. Within the 100-km region from the array center, 18 earthquakes with magnitude $M_v \geq 1.0$ are missed. We manually inspect two missed earthquakes with the largest magnitude ($M_v = 1.4$ and $M_v = 1.3$, respectively) in more detail and seek to answer whether these omissions are caused by the deficiency of proposed detectors or the limitation of OBDAS recording capability. We also include a detected small local earthquake ($M_v = 1.0$) for comparison. We first compute the theoretical arrival time of three earthquakes to the collocated SOB3 with the PREM model and confirm that they are all recorded by the OBS with good SNR in 1-8 Hz (red curves in Fig. 12A-D), which is the same frequency band for WSS/SSS detection. We also observe that the peak amplitude of the detected event is higher than that of missed events, regardless of its smaller magnitude and similar propagation distance.

We then examine the waveforms of the OBDAS, wherein we extract 30-second segments centered around the theoretical arrival time at each channel (waveforms at channel 7300 are shown with black curves in Fig. 12B-G). We apply the same set of Gaussian filters as in Fig. 3 to inspect channel-wise frequency contents. Fig. 12 H-J illustrates the SNR pattern with respect to channel number and frequency. Notably, the subsection at the beginning of the OBDAS array (i.e., channel 300-800) consistently exhibits high SNR across all three events. We postulated this is caused by long-lasting non-earthquake signals in the region. Further discussion on this topic is provided in section 5.3. Nevertheless, the SNR of the detected event (panel H) has two regions with noticeably high SNR, which are highlighted by red rectangles. These subsections successfully trigger the WSS detection on this event, although we observe that these regions have frequency contents different from the predefined 1-8 Hz range. Fig. 12E shows the waveforms filtered between the 3-7 Hz band, which has more visible arrivals than the waveforms in Fig. 12B. However, the two missed earthquakes do not exhibit such an SNR trend in any subsection of the array, and the waveforms of OBDAS are still below SNR regardless of frequency bands.

Based on these observations, we find that adapting to different frequency bands can improve the signal quality and facilitate a more detailed inspection. The constant 1-8 Hz band might be insufficient for capturing smaller-magnitude earthquakes as they tend to possess concentrated energy in a higher frequency band. However, it is noticeable that the two aforementioned undetected earthquakes remain absent from the OBDAS recordings, regardless of the chosen frequency bands. This phenomenon is also validated by their lower peak amplitudes on the OBS recordings. As the undetected earthquakes are of larger magnitudes and similar hypocentral distance than the recorded event, the smaller amplitudes can possibly be attributed to heterogeneous ground structures and a potentially larger attenuation factor at the south side of the cable than that of the north side (Viens, Perton, et al., 2022). Nevertheless, we can conclude that the missed earthquakes are caused by the limitation of OBDAS recording capability, rather than the ineffectiveness of proposed detection workflows.

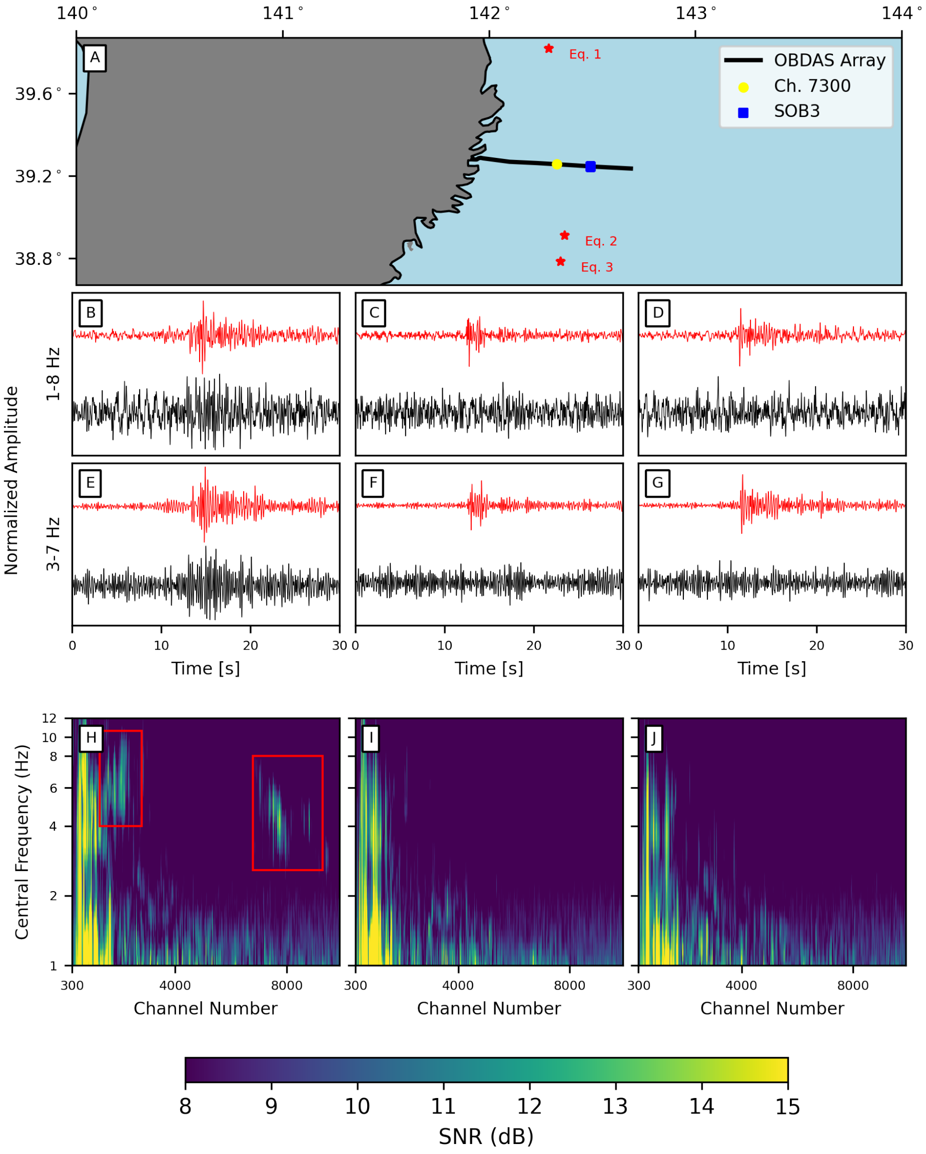

Figure 12: Analysis of undetected earthquakes. (A) Map showing the epicenters of a recorded earthquake (Eq. 1: 2019-11-24T02:02:12, 39.819N, 142.288 E, depth 26.4 km, $M_v = 1.0$), and two undetected earthquakes (Eq. 2: 2019-11-24,02:07:31 JST,38.786 N,142.345 E, depth 23.7 km, $M_v = 1.4$; Eq. 3: 2019-11-27,02:03:29 JST, 38.913 N, 142.365 E, depth 35.9 km, $M_v = 1.3$). Epicenters are represented by red stars, whereas channel 7300 and SOB3 are highlighted by a yellow circle and a blue rectangle, respectively. (B-D) Waveforms of Eq. 1,2,3 on SOB3 (red curve) and channel 7300 (black curve), respectively. Waveforms are bandpass filtered between 1-8 Hz. Waveform amplitudes are normalized with Eq. 1 peak amplitude. (E-G) Same as (B-D) but filtered between 3-7 Hz band. (H-J) SNR of Eq. 1,2,3 waveforms bandpass-filtered with a series of narrow-band Gaussian filters at each channel (Same filter as in Fig. 3). The red square in (H) highlights a region of high SNR corresponding to the detection subsection.

5.3 Uncataloged Detections

Our proposed workflow detects and associates the cataloged events recorded by OBDAS. At the same time, the remaining thousands of new detections do not match with a cataloged counterpart. As the result, we identify these detections as uncataloged local events. We focus on WSS detections which yield more accurate detection times to extract weak signals. WSS detects 9513 uncataloged events that were recorded by an average of 102 channels (i.e., $\geq$1010 m). Fig. 13A shows the number of uncataloged events detected by each channel. A strong spatial clustering pattern is observed with multiple identifiable subsections with significantly higher amounts of detections.

We first investigate the events recorded by channel 3078, which is the channel with the most uncataloged detection in the middle subsection of the array. We then compute the Cross-Correlation Coefficients (CCC) of stacked waveforms between each event pair. We observe that among all 1279 uncataloged events recorded by this channel, 30.3% (i.e., 387) of them show a strong waveform correlation with each other ($CCC \geq 0.6$, Fig. 13C). While most of the uncataloged events are of lower SNR, we then stack the waveforms of these events to increase the signal quality for each event. Two arrivals with high SNR emerge after stacking (Fig. 13D). The highly similar waveforms and consistent time moveouts between the two arrivals both suggest a repeating nature of these events, from a similar origin close to the channel 3078 of the fiber-optic array.

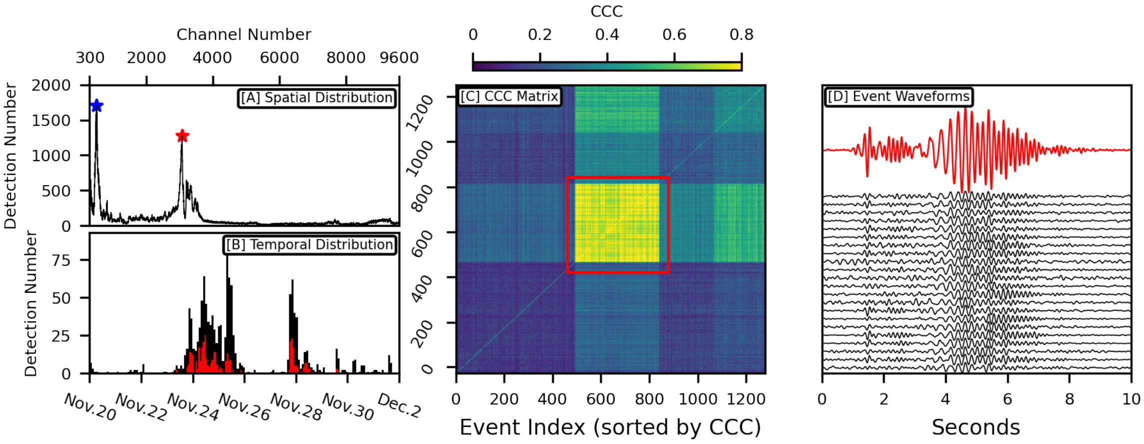

Figure 13: Examples of uncataloged detections. (A) Spatial distribution of uncataloged events across channels. The red star represents channel 3078, which has the most uncataloged events recorded in the middle section of the cable. The blue star represents channel 503, which is analyzed in the subsequent analysis. (B) A histogram showing the temporal distribution of the uncataloged events recorded by channel 3078. Black bars depict the distribution of all uncataloged events detected by the channel, whereas red bars only include high-CCC events used for stacking in panel (D). (C) Cross-correlation Coefficient (CCC) matrix of events recorded by channel 3078. The patch highlighted by the red rectangle represents the events with high CCC between each other. (D) Waveforms of uncataloged events at channel 3078. Black waveforms represent individual events, while the red waveform is stacked using all high-CCC events.

Similarly, we look at another subsection with a substantial number of uncataloged detections. At the starting end of the array, channel 503 has the most detections (blue star in Fig. 13A). Uncataloged detections from this subsection do not exhibit a repetitive pattern and no clear arrivals are observed in the waveforms. In addition, we find that uncataloged events from this subsection exhibit a strong temporal clustering pattern (Fig. 14A). Their waveforms cannot be well separated, instead, they blend together without a clear start or end point, resembling a continuous stream of events (Fig. 14B). Periods with streams of uncataloged events coincide with periods with consistent energy in the 3-5 Hz domain. Similar observations have also been reported in a previous study and might be due to sediment transports or meteorological-related signals ((Lindsey et al., 2019)). We attribute these signals to be the cause of the smeared SNR in the near-shore channels observed in Fig. 12.

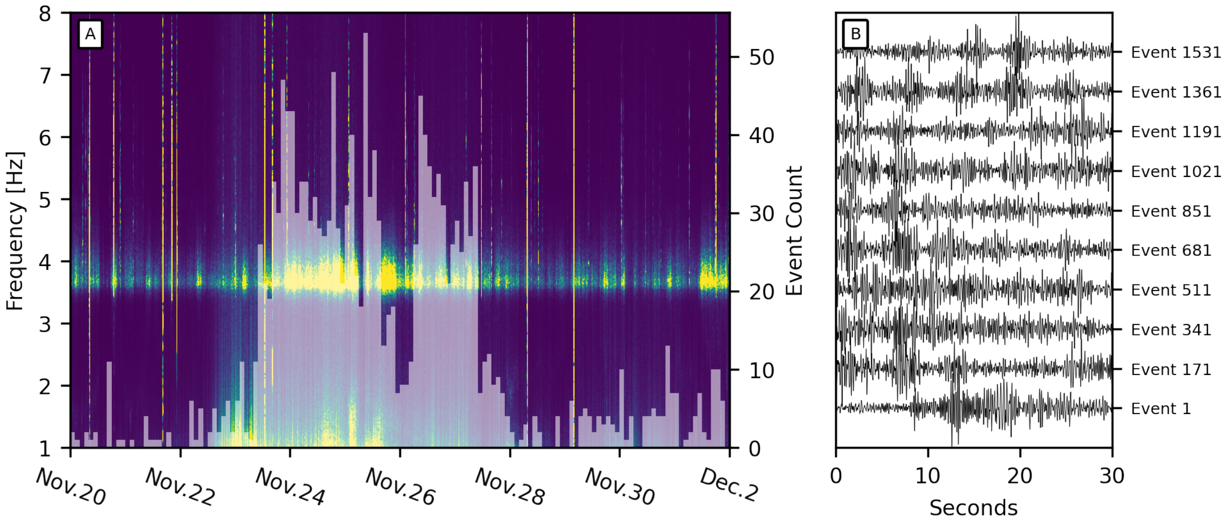

Figure 14: Temporal distribution and selected waveforms of uncataloged detections from channel 503. (A) A spectrogram of the 12-day continuous time series of channel 503. White bars represent a histogram showing the temporal distribution of the uncataloged events of the channel. (B) Waveforms of selected uncataloged events of channel 503. All waveforms are bandpass-filtered between 3-8 Hz.

5.4 Implications for the recording capability of the Sanriku OBDAS array

Our results demonstrate the earthquake recording capability of the Sanriku OBDAS shows strong variation over different sections. Despite this feature, we summarize its overall recording capability by integrating detection results from all analyzed channels of both detection methods. In Fig. 15, we show the detection completeness under two different criteria. Fig. 15A and B show the detection completeness trends by only considering associated cataloged events. These statistics describe the performance of the OBDAS in terms of recording earthquakes with large theoretical amplitudes. The steady decreasing trend in cumulative detection rate at the first 200 km range suggests that the OBDAS is more powerful in capturing local events ($< 200km$, Fig. 15A). After 200 km, the cumulative detection completeness rate remains relatively constant. This observation can be attributed to the bias of the theoretical amplitude threshold, as it excludes most small-magnitude earthquakes far away from the cable. Fig. 15C, D shows the overall detection statistics with respect to all earthquakes on the JMA catalog. The detection completeness rate monotonically decreases with epicentral distance, as expected. Comparing the median cataloged magnitude curve in panel C with the median detected magnitude curve in panel A, we find a similar trend for the first 200 km. This suggests that the OBDAS recording performance is comparable to the JMA network on a regional scale. Fig. 15D illustrates that the most missed earthquakes are small-magnitude events, and the OBDAS recorded most of $M_v > 3$ earthquakes.

Therefore, considering these statistics and previously discussed uncataloged detections (section 5.3), we conclude that the Sanriku OBDAS array exhibits strong capabilities in recording local earthquakes, as well as recording medium-to-large earthquakes ($M_v > 3$) at a regional scale ($200-1000km$). Beyond recording cataloged events, on one hand, newly detected uncataloged events demonstrate the applicability of OBDAS as a good complement to existing instruments as it detects tiny events in previously under-sampled zones. OBDAS can contribute to improving existing catalogs. On the other hand, due to its good performance in recording large-magnitude events, together with its real-time data transmission feature, OBDAS can assist in advancing Earthquake Early Warning applications in coastal regions.

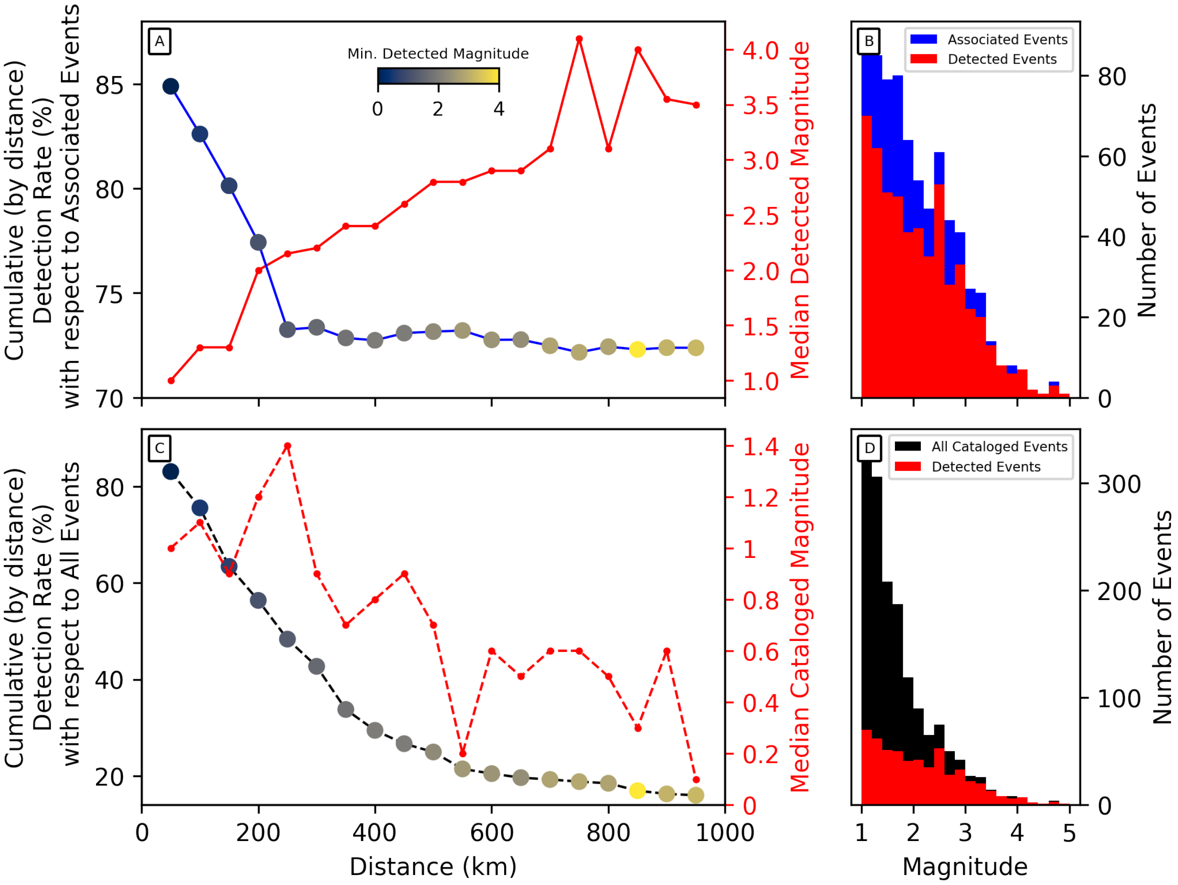

Figure 15: The distribution of recorded cataloged earthquakes by magnitude and epicentral distance. (A) Cumulative detection rates of associated events only and median magnitudes of detected events. Earthquakes are divided into subgroups by epicentral distances to the center of the OBDAS array, with 50-km increments. The blue curve (left vertical axis) shows the cumulative detection rate. The color of the dots scales with the minimum magnitude of all earthquakes in each subgroup. The red curve (right vertical axis) shows the median magnitude of detected earthquakes in each subgroup. (B) Number of detections by earthquake magnitude. Blue bars represent all associated earthquakes in different magnitude intervals, and the red bars represent the ones that are recorded by the OBDAS array. (C) Same as (A), but the detection rates are calculated with respect to all cataloged events, and the right vertical axis represents the median magnitude of all cataloged earthquakes in each subgroup. (D) Same as (B), but the black bars represent all cataloged earthquakes.

6 Conclusion

We assessed the recording capability of the Sanriku OBDAS array by conducting a detection analysis with 12 days of recordings. We utilized the spatial coherency of earthquake signals recorded by the OBDAS channels and propose two detection methods: waveform similarity search (WSS) and spectrum similarity search (SSS). We showed the efficacy of the proposed detectors by successfully detecting thousands of cataloged and uncataloged earthquakes. Our results indicated that the recording capability of the OBDAS array varies substantially across channels. Results also showed that the OBDAS array can record $\approx 80\%$ of cataloged regional earthquakes within a 100 km radius from the array, and can record $> 90\%$ of $M_v > 4$ earthquakes that are less than 1000 km away from the array. The OBDAS array is also capable of recording uncataloged events and repeating earthquakes among different spatial sub-regions.

Assessing the earthquake recording capability of the OBDAS array is a prerequisite of routine deployments of OBDAS for long-term seismic monitoring. Our study demonstrated that OBDAS has the potential to mitigate offshore seismic instrumentation scarcity by providing unprecedented spatial sampling with a suitable recording capability at a local-to-regional scale. Given the extensive networks of telecommunication fibers laid across the ocean floor, especially near subduction zones, OBDAS arrays possess a significant capacity to advance our comprehension of the Earth's interior and record dynamic ground motions in formerly under-sampled regions.

7 Open Research

Bathymetric data is available via GEBCO.OBS data is available via JMA ($https://www.jma.go.jp/jma/index.html$). Part of the OBDAS data and all code necessary to reproduce the findings will be shared on a public repository before the eventual acceptance of the paper.

Acknowledgments

Y.M. and A.S. were partially supported by the NSF award EAR2022716. Z.J.S. acknowledges support from the Air Force Research Laboratory grant FA9453-21-2-0018. We thank Fujitsu for collaborating with the University of Tokyo for DAS data collection.

References

Albright, S. C., Winston, W. L., Zappe, C. J., & Broadie, M. N. (2011). *Data analysis and decision making* (Vol. 577). Citeseer.

Allen, R. M., & Melgar, D. (2019). Earthquake early warning: Advances, scientific challenges, and societal needs. *Annu. Rev. Earth Planet. Sci.*, *47*(1), 361–388.

Baba, T., Cummins, P. R., & Hori, T. (2005). Compound fault rupture during the 2004 off the kii peninsula earthquake (m 7.4) inferred from highly resolved coseismic sea-surface deformation. *Earth, planets and space*, *57*(3), 167–172.

Bouffaut, L., Taweesintananon, K., Kriesell, H. J., Rørstadbotnen, R. A., Potter, J. R., Landrø, M., … others (2022). Eavesdropping at the speed of light: Distributed acoustic sensing of baleen whales in the arctic. *Frontiers in Marine Science*, 994.

Brune, J. N. (1970). Tectonic stress and the spectra of seismic shear waves from earthquakes. *J Geophys Res*, *75*(26), 4997–5009.

Cedilnik, G., Lees, G., Schmidt, P., Herstrøm, S., & Geisler, T. (2019). Ultra-long reach fiber distributed acoustic sensing for power cable monitoring. In *Proceedings of the jicable.*

Chamberlain, C. J., Hopp, C. J., Boese, C. M., Warren-Smith, E., Chambers, D., Chu, S. X., … Townend, J. (2018). Eqcorrscan: Repeating and near-repeating earthquake detection and analysis in python. *Seismological Research Letters*, *89*(1), 173–181.

Cheng, F., Chi, B., Lindsey, N. J., Dawe, T. C., & Ajo-Franklin, J. B. (2021). Utilizing distributed acoustic sensing and ocean bottom fiber optic cables for submarine structural characterization. *Scientific reports*, *11*(1), 1–14.

Chung, A. I., Meier, M.-A., Andrews, J., Böse, M., Crowell, B. W., McGuire, J. J., & Smith, D. E. (2020). Shakealert earthquake early warning system performance during the 2019 ridgecrest earthquake sequence. *Bulletin of the Seismological Society of America*, *110*(4), 1904–1923.

Delaney, J., & Kelley, D. (2015). Next-generation science in the ocean basins: Expanding the oceanographer's toolbox utilizing submarine electro-optical sensor networks. In *Seafloor observatories* (pp. 465–502). Springer.

Dessa, J.-X., Operto, S., Kodaira, S., Nakanishi, A., Pascal, G., Uhira, K., & Kaneda, Y. (2004). Deep seismic imaging of the eastern nankai trough, japan, from multifold ocean bottom seismometer data by combined travel time tomography and prestack depth migration. *Journal of Geophysical Research: Solid Earth*, *109*(B2).

Dziewonski, A. M., & Anderson, D. L. (1981). Preliminary reference earth model. *Physics of the earth and planetary interiors*, *25*(4), 297–356.

Farghal, N. S., Saunders, J. K., & Parker, G. A. (2022). The potential of using fiber optic distributed acoustic sensing (das) in earthquake early warning applications. *Bulletin of the Seismological Society of America*.

Fukushima, S., Shinohara, M., Nishida, K., Takeo, A., Yamada, T., & Yomogida, K. (2022). Detailed s-wave velocity structure of sediment and crust off sanriku, japan by a new analysis method for distributed acoustic sensing data using a seafloor cable and seismic interferometry. *Earth, Planets and Space*, *74*(1), 1–11.

Gebco 2021 grid, the general bathymetric chart of the oceans. (2021). Retrieved from `https://www.gebco.net/data_and_products/gridded_bathymetry_data/` doi: 10.5285/c6612cbe-50b3-0cff-e053-6c86abc09f8f

Geller, R. J. (1976). Scaling relations for earthquake source parameters and magnitudes. *B Seismol Soc Am*, *66*(5), 1501–1523.

Grattan, K., & Sun, T. (2000). Fiber optic sensor technology: an overview. *Sensors and Actuators A: Physical*, *82*(1-3), 40–61.

Hino, R., Tanioka, Y., Kanazawa, T., Sakai, S., Nishino, M., & Suyehiro, K. (2001). Micro-tsunami from a local interplate earthquake detected by cabled offshore tsunami observation in northeastern japan. *Geophysical research letters*, *28*(18), 3533–3536.

Howe, B. M., Angove, M., Aucan, J., Barnes, C. R., Barros, J. S., Bayliff, N., … others (2022). SMART subsea cables for observing the earth and ocean, mitigating environmental hazards, and supporting the blue economy. *Frontiers in Earth Science*, *9*, 775544.

Ide, S., Araki, E., & Matsumoto, H. (2021). Very broadband strain-rate measurements along a submarine fiber-optic cable off cape muroto, nankai subduction zone, japan. *Earth, Planets and Space*, *73*(1), 1–10.

Japan meteorological agency website. (n.d.). Retrieved from `https://www.data.jma.go.jp/svd/eqev/data/bulletin/index_e.html`

Japan oceanographic data center 500m gridded bathymetry data. (n.d.). Retrieved from `https://www.jodc.go.jp/jodcweb/JDOSS/infoJEGG.html`

Kanazawa, T., & Hasegawa, A. (1997). Ocean-bottom observatory for earthquakes and tsunami off Sanriku, north-east Japan using submarine cable, paper presented at international workshop on scientific use of submarine cables, comm. for sci. *Use of Submarine Cables, Okinawa, Japan.*

Kanazawa, T., Uehira, K., Mochizuki, M., Shinbo, T., Fujimoto, H., Noguchi, S., ... Sekiguchi, S. (2016). S-net project, cabled observation network for earthquakes and tsunamis. *Abstract WE2B–3, Presented at SubOptic 2016*, 18–21.

Kugler, S., Bohlen, T., Forbriger, T., Bussat, S., & Klein, G. (2007). Scholte-wave tomography for shallow-water marine sediments. *Geophysical Journal International*, *168*(2), 551–570.

Lay, T., Aster, R., Forsyth, D., Romanowicz, B., Allen, R., Cormier, V., ... others (2009). Seismological grand challenges in understanding earth's dynamic systems. *Report to the National Science Foundation, IRIS Consortium*, *46*, 1–18.

Leys, C., Ley, C., Klein, O., Bernard, P., & Licata, L. (2013). Detecting outliers: Do not use standard deviation around the mean, use absolute deviation around the median. *Journal of experimental social psychology*, *49*(4), 764–766.

Li, Z., Shen, Z., Yang, Y., Williams, E., Wang, X., & Zhan, Z. (2021). Rapid response to the 2019 ridgecrest earthquake with distributed acoustic sensing. *AGU Advances*, *2*(2), e2021AV000395.

Li, Z., & Zhan, Z. (2018). Pushing the limit of earthquake detection with distributed acoustic sensing and template matching: a case study at the brady geothermal field. *Geophysical Journal International*, *215*(3), 1583–1593.

Lindsey, N. J., Dawe, T. C., & Ajo-Franklin, J. B. (2019). Illuminating seafloor faults and ocean dynamics with dark fiber distributed acoustic sensing. *Science*, *366*(6469), 1103–1107.

Lindsey, N. J., Rademacher, H., & Ajo-Franklin, J. B. (2020). On the broadband instrument response of fiber-optic DAS arrays. *Journal of Geophysical Research: Solid Earth*, *125*(2), e2019JB018145.

Lindsey, N. J., Yuan, S., Lellouch, A., Gualtieri, L., Lecocq, T., & Biondi, B. (2020). City-scale dark fiber das measurements of infrastructure use during the covid-

19 pandemic. *Geophysical research letters*, *47*(16), e2020GL089931.

Lior, I., Sladen, A., Rivet, D., Ampuero, J.-P., Hello, Y., Becerril, C., … Christos, M. (2021). On the Detection Capabilities of Underwater Distributed Acoustic Sensing. *Journal of Geophysical Research: Solid Earth*, *126*(3), e2020JB020925. doi: 10.1029/2020JB020925

Lomax, A., Michelini, A., Curtis, A., & Meyers, R. (2009). Earthquake location, direct, global-search methods. *Encyclopedia of complexity and systems science*, *5*, 2449–2473.

Martin, E. R., Lindsey, N., Ajo-Franklin, J., & Biondi, B. (2018). Introduction to interferometry of fiber optic strain measurements. *EarthArXiv*. doi: 10.31223/osf.io/s2tjd

Mordret, A., Shapiro, N. M., Singh, S. S., Roux, P., & Barkved, O. I. (2013, March). Helmholtz tomography of ambient noise surface wave data to estimate Scholte wave phase velocity at Valhall life of the field. *GEOPHYSICS*, *78*(2), WA99–WA109. Retrieved 2014-02-27, from `http://library.seg.org/doi/abs/10.1190/geo2012-0303.1` doi: 10.1190/geo2012-0303.1

Muir, J., Fernando, B., & Barrett, E. (2023). False positives are common in single-station template matching. *Seismica*, *2*(2).

Nayak, A., Ajo-Franklin, J., & Team, I. V. D. F. (2021a). Distributed acoustic sensing using dark fiber for array detection of regional earthquakes. *Seismological Society of America*, *92*(4), 2441–2452.

Nayak, A., Ajo-Franklin, J., & Team, I. V. D. F. (2021b). Measurement of surface-wave phase-velocity dispersion on mixed inertial seismometer–distributed acoustic sensing seismic noise cross-correlations. *Bulletin of the Seismological Society of America*, *111*(6), 3432–3450.

Rivet, D., de Cacqueray, B., Sladen, A., Roques, A., & Calbris, G. (2021). Preliminary assessment of ship detection and trajectory evaluation using distributed acoustic sensing on an optical fiber telecom cable. *The Journal of the Acoustical Society of America*, *149*(4), 2615–2627.

Salaree, A., Howe, B. M., Huang, Y., Weinstein, S. A., & Sakya, A. E. (2023). A numerical study of SMART Cables potential in marine hazard early warning for the Sumatra and Java regions. *Pure Appl. Geophys.*, *180*(5), 1717–1749. (**doi:** 10.1007/s00024-022-03004-0)

Salaree, A., Spica, Z., & Huang, Y. (2023). Solving a seismic mystery with the audio from a diver's camera: The 2022 earthquake sequence in the Persian Gulf region. *Geophys. Res. Lett.*, *50*, e2023GL104544. (**doi:** 10.1029/2023GL104544)

Shinohara, M., Yamada, T., Akuhara, T., Mochizuki, K., & Sakai, S. (2022). Performance of seismic observation by distributed acoustic sensing technology using a seafloor cable off sanriku, japan. *Frontiers in Marine Science*, 466.

Shinohara, M., Yamada, T., Akuhara, T., Mochizuki, K., Sakai, S., Hamakawa, M., ... Kubota, S. (2019). Distributed acoustic sensing measurement by using seafloor optical fiber cable system off Sanriku for seismic observation. In *Oceans 2019 MTS/IEEE Seattle* (pp. 1–4). doi: 10.23919/OCEANS40490.2019.8962757

Shinohara, M., Yamada, T., Kanazawa, T., Hirata, N., Kaneda, Y., Takanami, T., ... others (2004). Aftershock observation of the 2003 tokachi-oki earthquake by using dense ocean bottom seismometer network. *Earth, planets and space*, *56*(3), 295–300.

Shinohara, M., Yamada, T., Sakai, S., Shiobara, H., & Kanazawa, T. (2016). Development and installation of new seafloor cabled seismic and tsunami observation system using ICT. In *Oceans 2016 mts/ieee monterey* (pp. 1–4).

Sladen, A., Rivet, D., Ampuero, J.-P., De Barros, L., Hello, Y., Calbris, G., & Lamare, P. (2019). Distributed sensing of earthquakes and ocean-solid earth interactions on seafloor telecom cables. *Nature Communications*, *10*(1), 1–8.

Spica, Z. J., Castellanos, J. C., Viens, L., Nishida, K., Akuhara, T., Shinohara, M., & Yamada, T. (2022). Subsurface imaging with ocean-bottom distributed acoustic sensing and water phases reverberations. *Geophysical Research Letters*, e2021GL095287.

Spica, Z. J., Perton, M., Martin, E. R., Beroza, G. C., & Biondi, B. (2020). Urban seismic site characterization by fiber-optic seismology. *Journal of Geophysical Research: Solid Earth*, *125*(3), e2019JB018656. doi: 10.1029/2019JB018656

Thurber, C. H., & Engdahl, E. R. (2000). Advances in global seismic event location. In *Advances in seismic event location* (pp. 3–22). Springer.

Tonegawa, T., Fukao, Y., Nishida, K., Sugioka, H., & Ito, A. (2013). A temporal change of shear wave anisotropy within the marine sedimentary layer associated with the 2011 Tohoku-Oki earthquake. *Journal of Geophysical Research:*

Solid Earth, *118*(2), 607–615.

Ugalde, A., Becerril, C., Villaseñor, A., Ranero, C. R., Fernández-Ruiz, M. R., Martin-Lopez, S., … Martins, H. F. (2022). Noise levels and signals observed on submarine fibers in the canary islands using das. *Seismological Research Letters*, *93*(1), 351–363.

van den Ende, M., & Ampuero, J.-P. (2021). Evaluating seismic beamforming capabilities of distributed acoustic sensing arrays. *Solid Earth*, *12*(4), 915–934.

Viens, L., Bonilla, L. F., Spica, Z. J., Nishida, K., Yamada, T., & Shinohara, M. (2022). Nonlinear earthquake response of marine sediments with distributed acoustic sensing. *Geophysical Research Letters*, *49*(21), e2022GL100122. doi: https://doi.org/10.1029/2022GL100122

Viens, L., Perton, M., Spica, Z. J., Nishida, K., Yamada, T., & Shinohara, M. (2022). Understanding surface-wave modal content for high-resolution imaging of submarine sediments with distributed acoustic sensing. *Geophysical Journal International*. doi: 10.1093/gji/ggac420

Wang, H. F., Zeng, X., Miller, D. E., Fratta, D., Feigl, K. L., Thurber, C. H., & Mellors, R. J. (2018). Ground motion response to an ml 4.3 earthquake using co-located distributed acoustic sensing and seismometer arrays. *Geophysical Journal International*, *213*(3), 2020–2036.

Williams, E. F., Fernández-Ruiz, M. R., Magalhaes, R., Vanthillo, R., Zhan, Z., González-Herráez, M., & Martins, H. F. (2019). Distributed sensing of microseisms and teleseisms with submarine dark fibers. *Nature communications*, *10*(1), 1–11.

Williams, E. F., Fernández-Ruiz, M. R., Magalhaes, R., Vanthillo, R., Zhan, Z., González-Herráez, M., & Martins, H. F. (2021). Scholte wave inversion and passive source imaging with ocean-bottom das. *The Leading Edge*, *40*(8), 576–583.

Williams, E. F., Zhan, Z., Martins, H. F., Fernandez-Ruiz, M. R., Martin-Lopez, S., Gonzalez-Herraez, M., & Callies, J. (2022). Surface gravity wave interferometry and ocean current monitoring with ocean-bottom das. *Journal of Geophysical Research: Oceans*, e2021JC018375.

Xiao, H., Tanimoto, T., Spica, Z. J., Gaite, B., Ruiz-Barajas, S., Pan, M., & Viens, L. (2022). Locating the precise sources of high-frequency microseisms using distributed acoustic sensing. *Geophysical Research Letters*, *49*(17), e2022GL099292.

Yin, J., Zhu, W., Li, J., Biondi, E., Miao, Y., Spica, Z. J., … others (2023). Earthquake magnitude with das: A transferable data-based scaling relation. *Geophysical Research Letters*, *50*(10), e2023GL103045.

Yoon, C. E., O'Reilly, O., Bergen, K. J., & Beroza, G. C. (2015). Earthquake detection through computationally efficient similarity search. *Science advances*, *1*(11), e1501057.

Zeng, X., Bao, F., Thurber, C. H., Lin, R., Wang, S., Song, Z., & Han, L. (2022). Turning a telecom fiber-optic cable into an ultradense seismic array for rapid postearthquake response in an urban area. *Seismological Society of America*, *93*(2A), 853–865.

Zhan, Z. (2020). Distributed acoustic sensing turns fiber-optic cables into sensitive seismic antennas. *Seismological Research Letters*, *91*(1), 1–15.

Zhu, W., Biondi, E., Li, J., Yin, J., Ross, Z. E., & Zhan, Z. (2023). Seismic arrival-time picking on distributed acoustic sensing data using semi-supervised learning. *arXiv preprint arXiv:2302.08747*.

Supporting Information for Assessing the Earthquake Recording Capability of an Ocean-bottom Distributed Acoustic Sensing Array in the Sanriku region, Japan

Yaolin Miao[1], Amir Salaree[1], Zack J. Spica[1], Kiwamu Nishida[2], Tomoaki Yamada[2], Masanao Shinohara[2]

[1]Department of Earth and Environmental Sciences, University of Michigan, Ann Arbor, Michigan, USA

[2]Earthquake Research Institute, The University of Tokyo, Tokyo, Japan

Contents of this file

Text S1 WSS detects thousands of repeating events exclusively near ch.200-300. These repeating signals are of short durations of 1-2 seconds and have a similar frequency content as local earthquakes in the 1-8 Hz domain. However, the consistent detection of the specific section implies a possibility of a different source other than natural seismicity. As a result, we exclude this segment from seismicity detection analysis and detect these events using conventional Template Matching (TM). TM results show that these signals exhibit a strong daily pattern, and daily maximums are constantly in the mornings of local time, which potentially indicates an anthropogenic inducement.

Figure S1 Epicenters of earthquakes that are included in the SNR analysis.

Figure S2 Peak Ground Acceleration (PGA) of the 35 manually picked earthquakes (one clipped earthquake is excluded) recorded by the OBS station and OBDAS ch.10,265 after bandpass filtered between 0.5 and 12 Hz.

Figure S3 Repeating events recorded near ch.200.

Figure S4 Distribution of selected Hi-net stations and earthquakes for extracting external waveforms for SSS.

Figure S5 A synthetic test of WSS with boxcar signals.

Figure S6 Histogram showing the WSS detection number as a function of the N parameter.

Figure S7 Histogram of the distribution of the number of high-coherence channels of all time windows.

Figure S8 Travel time uncertainty synthesis.

Figure S9 A map showing included and excluded events by theoretical amplitude threshold.

Figure S10 Dispersion analysis of tails of two earthquake waveforms.

Table S1 Recording time, latitude, longitude, distance, and back azimuth from the center of the OBDAS array, and average SNR of earthquakes used for the SNR analysis.

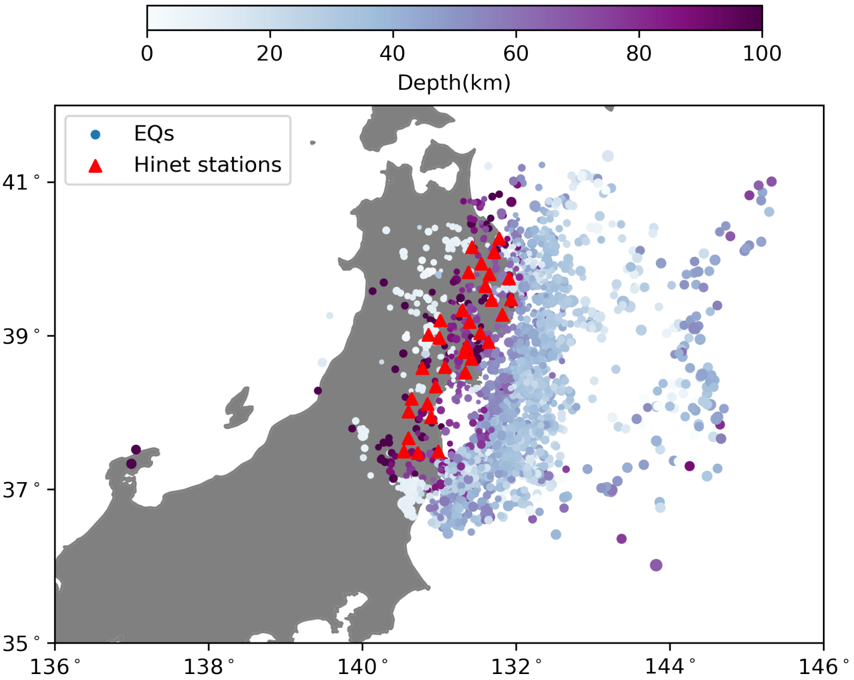

Figure S1: (A). Distribution of the 36 selected earthquakes for SNR analysis. The star size scales with earthquake magnitudes. (B) The same distribution is shown on a rose map. Polar angles represent back azimuth between the center of the OBDAS array and earthquake epicenters. Distance caps at 500 km. The colors of dots correspond to earthquake magnitudes.

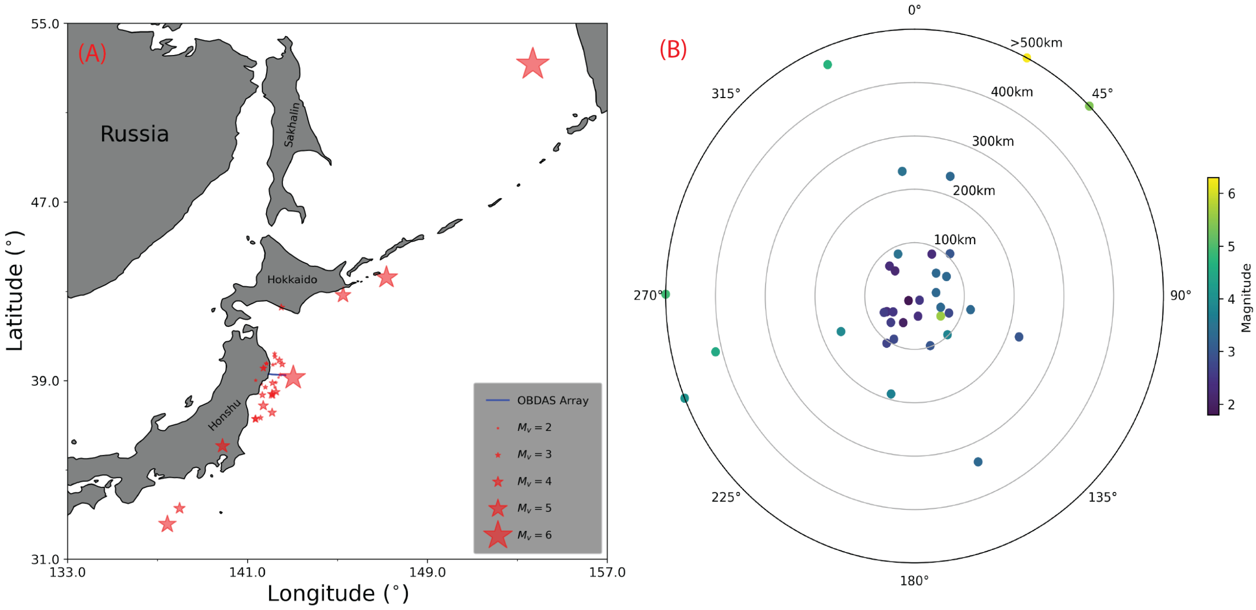

Figure S2: Peak Ground Acceleration (PGA) of the 35 manually picked earthquakes (one clipped earthquake is excluded) recorded by the OBS station and the nearest OBDAS channel 10,265, after bandpass filtered between 0.5 and 8 Hz. PGA is displayed as a discrete function of azimuth between earthquake epicenters and the middle of the OBDAS array. Zero azimuth means north.

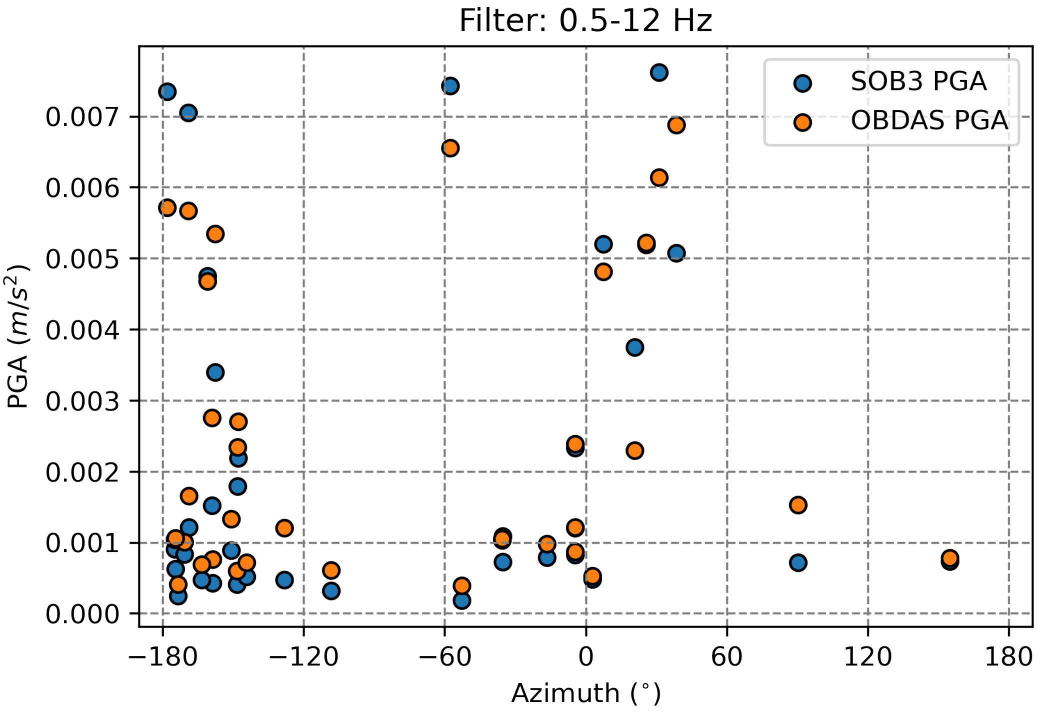

Figure S3: Repeating events recorded near ch.200. (A) Waveforms of a sample event across channels; (B) temporal distribution of such events.

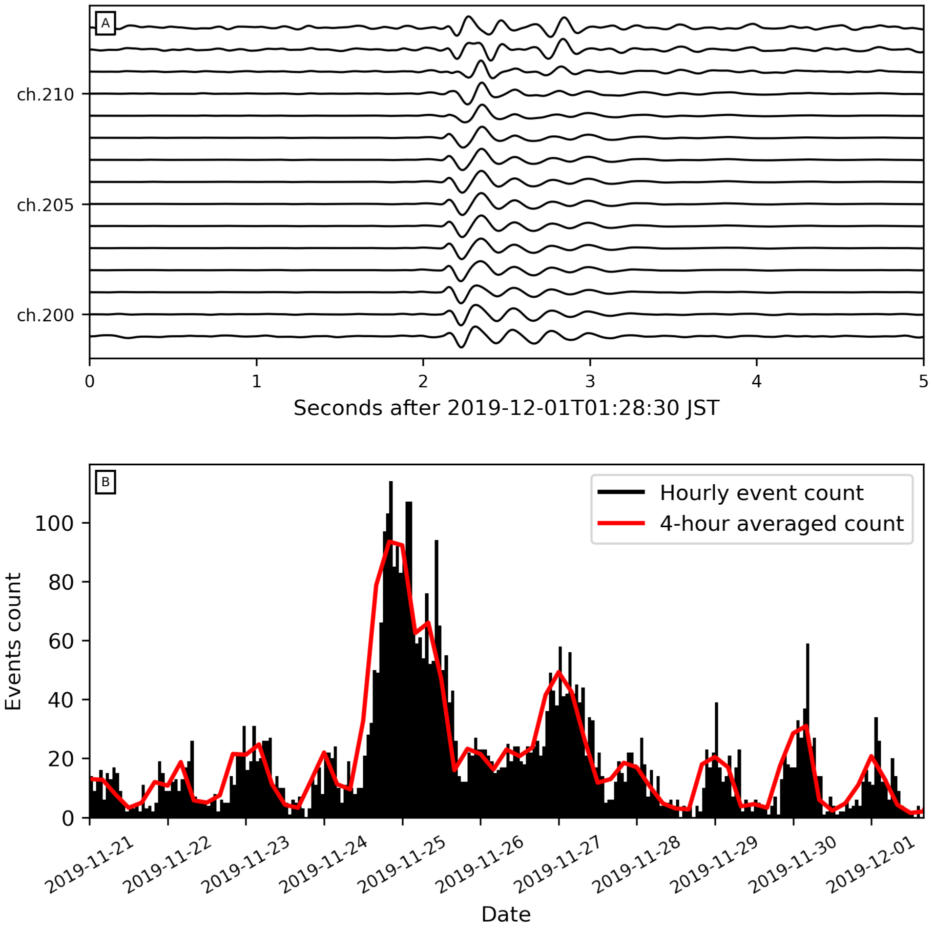

Figure S4: Distribution of selected Hi-net stations and earthquakes for extracting external waveforms for SSS. Selected Hinet stations are represented by red triangles and the chosen earthquakes are shown with purple circles, with their color scales with earthquake depth.

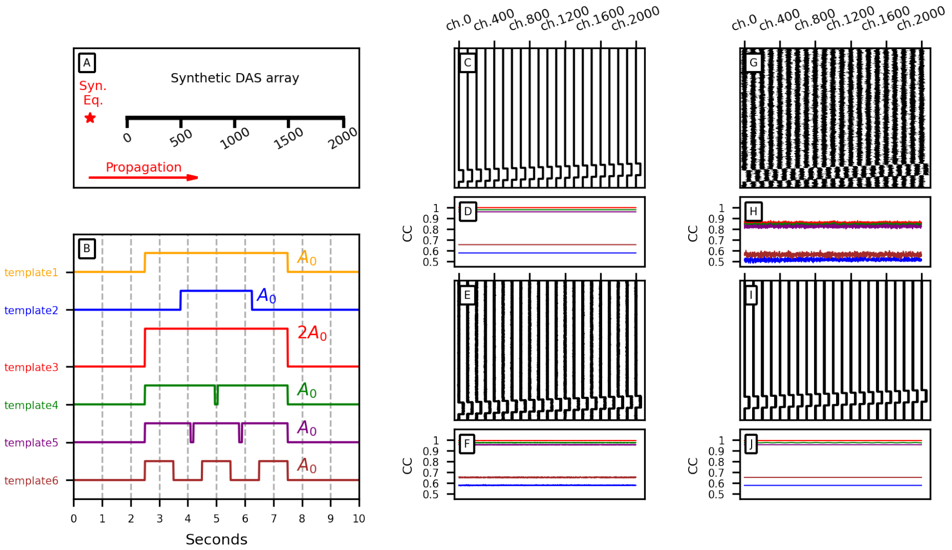

Figure S5: A synthetic test of WSS with boxcar signals. (A) An illustrative map showing the synthetic cable with 2,000 channels and a g-meter channel spacing. An imaginary source is represented as the red star, and seismic waves are assumed to propagate along the array. (B) Waveforms of seven synthetic templates, which are comprised of boxcar signals of different durations and amplitudes. (C, E, G, I) Synthetic DAS waveforms across channels with four different types of ambient noise, assuming a constant apparent velocity. Synthetic earthquake waveform is also represented by a boxcar signal (identical to template 1 in panel (B)). (D, F, H, J) Cross-correlation of synthetic DAS recordings (panel C, E, G, I) with prebuilt synthetic templates across channels. The color of the cross-correlation curves corresponds to the same color as shown in panel (B).

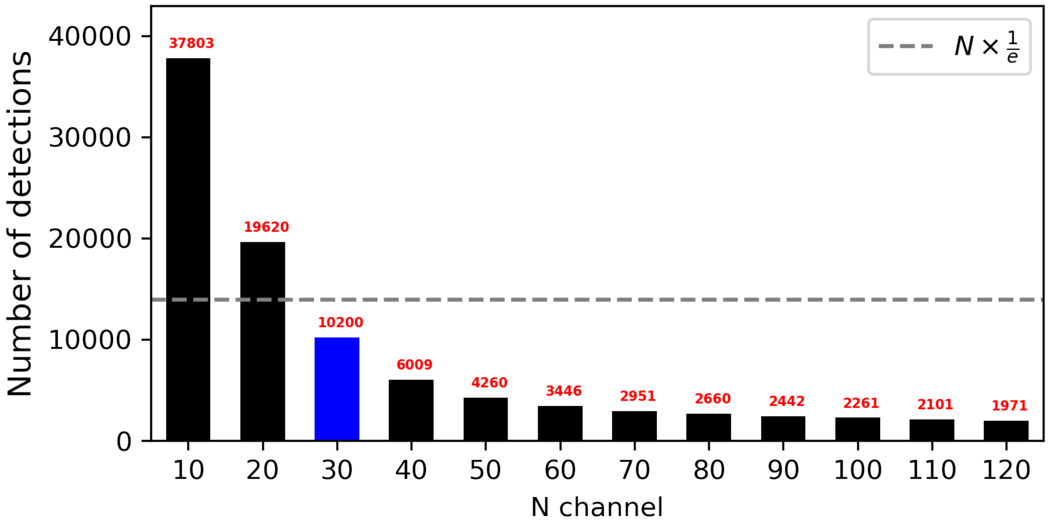

Figure S6: Histogram showing the WSS detection number as a function of the N parameter. The grey dashed line is the thresholding line of $\frac{1}{e}$ of the maximum detection number. $N = 30$ is adopted for the subsequent analysis.

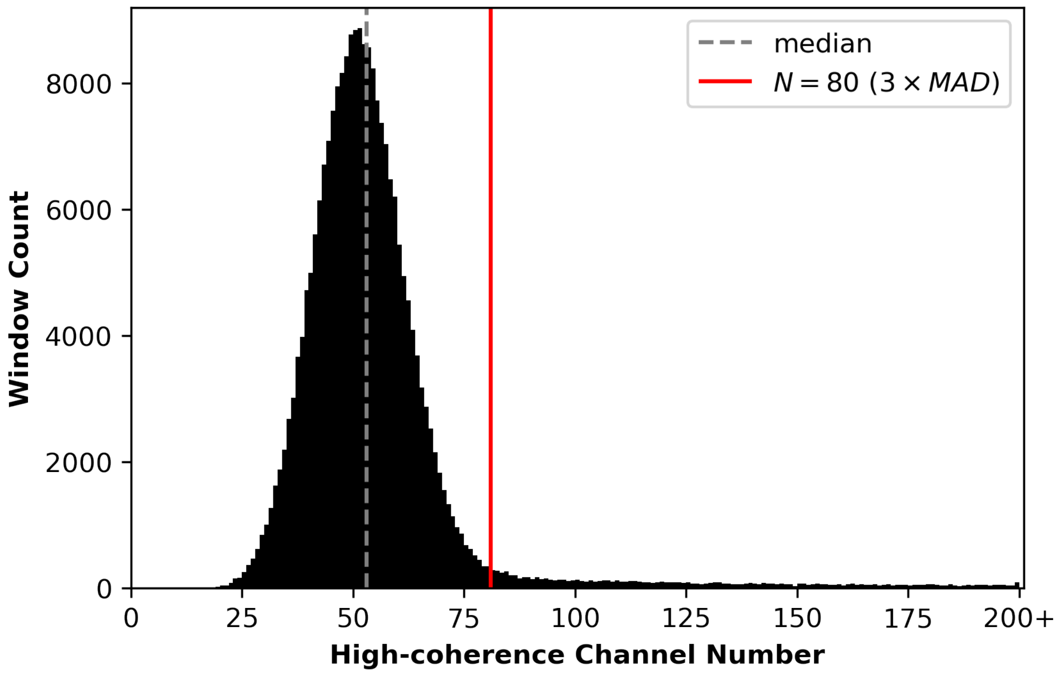

Figure S7: Histogram of the distribution of the number of high-coherence channels of all time windows. The grey dashed line represents the median value of 52. The red vertical line represents the chosen threshold of $3 \times MAD$.

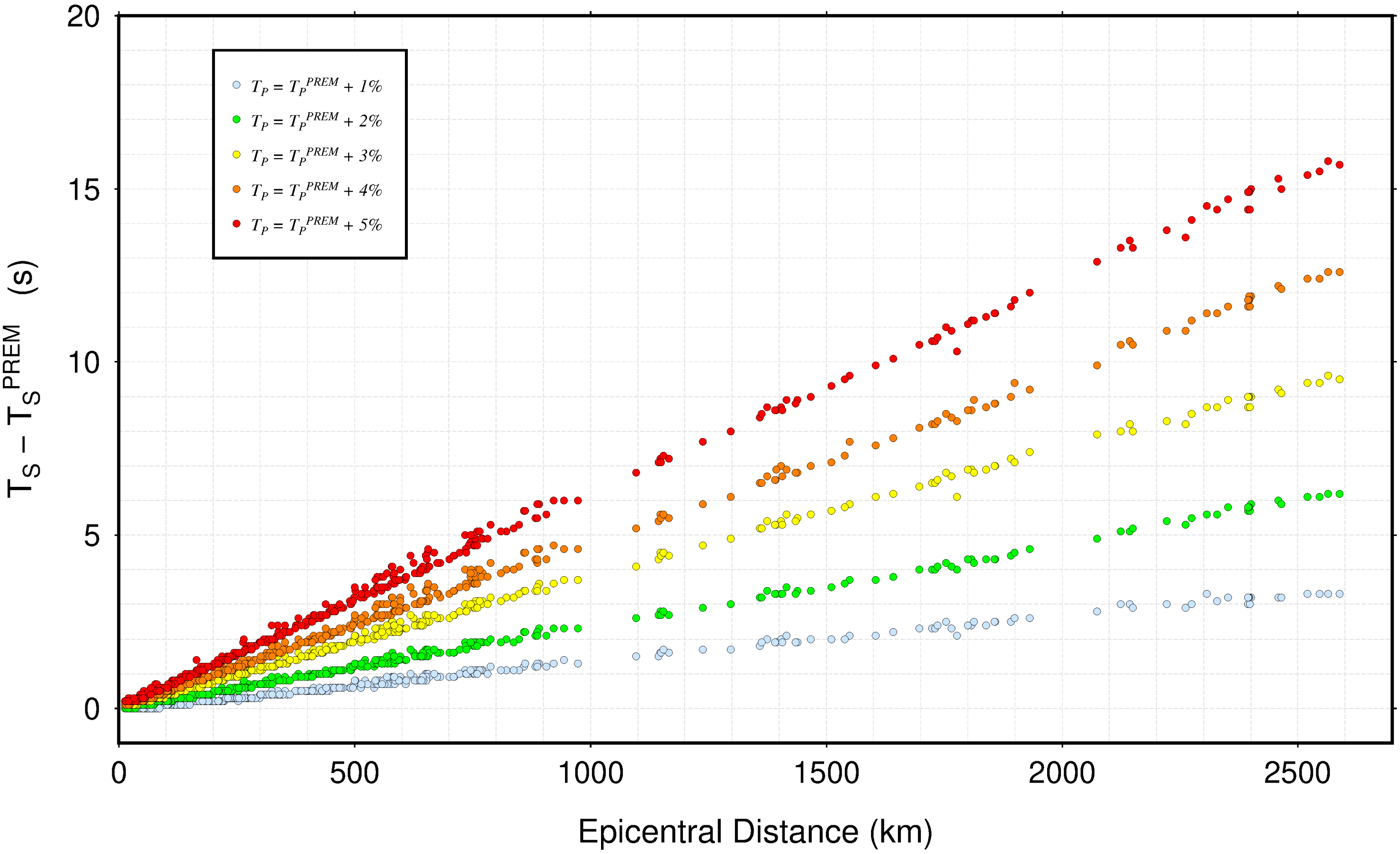

Figure S8: A synthesis on travel time calculation based on different velocity models. The base model (in light blue color) is the PREM model used in this study. Curves of other colors represent different models after different levels of perturbation to the PREM model.

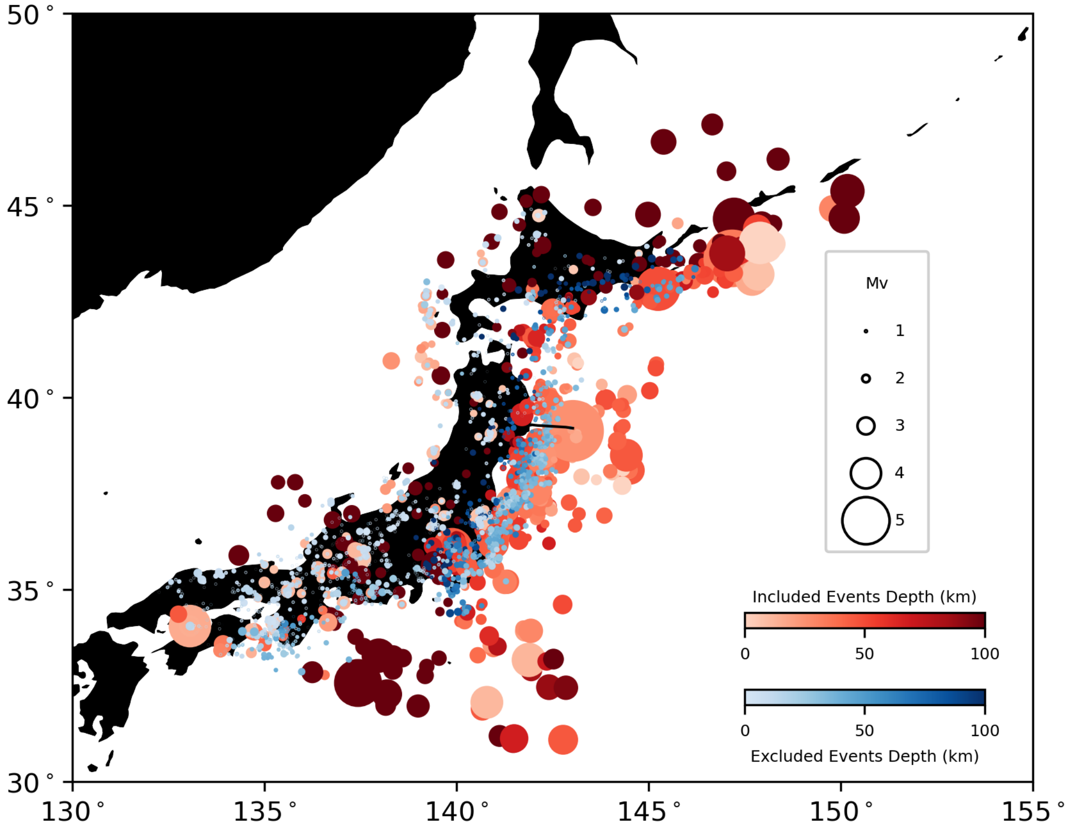

Figure S9: A map showing included and excluded events by theoretical amplitude threshold. The circles in red are the cataloged events that passed the theoretical amplitude threshold and are included in the association process, while the ones in blue are the events that failed the threshold and are excluded from the subsequent analysis. The color of the circles scales with event depth and the size of the circles scales with event magnitude.

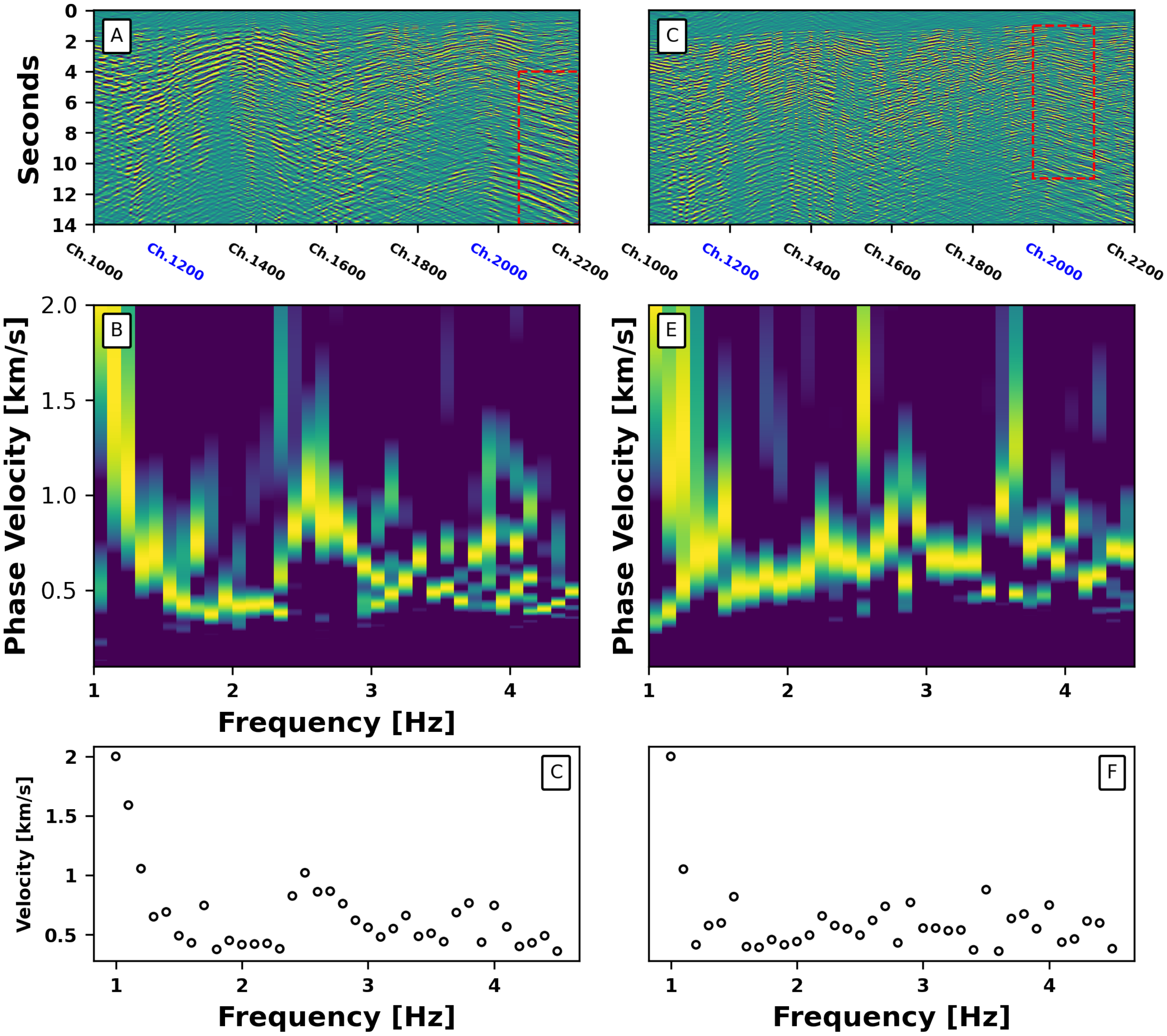

Figure S10: Dispersion analysis of tails of two earthquake waveforms. (A, C) OBDAS recordings across channels. Red rectangles highlight the waveforms selected to conduct the dispersion analysis for the two earthquakes, respectively. (B, E) Dispersion matrices of the two earthquakes after radon transform. (C, F) Extracted dispersion curves of tails of two earthquake waveforms, respectively. The curve in panel (C) has a two-mode dispersion pattern, which possibly indicates the tail to be surface waves, while the dispersion curve in panel (F) does not exhibit this pattern.

Table S1: Recording time, latitude, longitude, distance, and back azimuth from the center of the OBDAS array, and average SNR of earthquakes used for the SNR analysis.

No.	Time (UTC)	Latitude	Longitude	Distance (km)	Back azimuth	M_v	Average SNR (db)
1	2019-11-20 06:43:22.25	39.011	141.362	86.3	251.86	2.3	9.55
2	2019-11-20 07:44:04.18	39.59	141.736	61.69	306.93	2.2	7.52
3	2019-11-20 08:26:07.50	53.162	153.685	1772.33	25.59	6.3	12.74
4	2019-11-20 21:38:05.08	39.257	142.452	12.19	90.13	2.5	12.2
5	2019-11-20 21:57:29.68	39.733	142.539	56.43	20.34	3.3	14.44
6	2019-11-21 03:30:00.66	40.072	142.221	90.94	355.18	2.8	9.28
7	2019-11-21 16:29:13.98	38.391	142.093	98.19	191.18	3.8	19.45
8	2019-11-21 16:33:21.54	38.392	142.085	98.21	191.59	3	12.09
9	2019-11-21 20:23:49.95	36.071	139.891	413.47	211.86	4.5	6.55
10	2019-11-21 22:31:57.08	32.564	137.438	863.92	212.1	4.9	11.04
11	2019-11-22 18:50:55.87	42.274	142.5	335.92	2.67	3.3	6.65
12	2019-11-23 07:01:06.17	38.913	142.265	38.5	185.89	2.4	9.45
13	2019-11-23 12:58:09.99	43.618	147.179	632.27	38.45	5.4	9.25
14	2019-11-23 16:22:03.40	39.55	141.706	61.31	302.16	3.3	18.11
15	2019-11-23 22:40:51.62	37.28	141.359	235.11	201.07	3.5	12.49
16	2019-11-24 20:12:37.30	39.761	141.842	68.96	324.38	2.6	9.14
17	2019-11-25 01:41:03.28	37.878	141.704	162.23	199.23	3.9	16.26
18	2019-11-26 02:25:55.86	38.895	142.113	43.76	203.08	3.3	16.93
19	2019-11-26 03:09:31.75	39.749	142.254	54.9	354.93	2	8.79
20	2019-11-26 06:18:20.80	37.281	141.339	235.63	201.49	3.3	6.29
21	2019-11-27 04:57:04.43	38.349	141.663	115.58	209.36	3.3	11.64
22	2019-11-27 11:38:33.33	39.916	142.415	73.81	6.97	3.3	16.71
23	2019-11-27 16:01:07.84	37.331	141.582	223.5	196.82	3	8.63
24	2019-11-27 20:24:36.10	33.277	137.979	770.06	211.7	4.1	6.39
25	2019-11-28 00:48:34.94	38.696	142.224	62.88	186.89	2.3	6.76
26	2019-11-28 07:41:15.49	42.826	145.249	467.19	30.99	4.7	10.36
27	2019-11-28 08:45:30.16	39.136	142.378	14.7	156.57	1.8	7.69
28	2019-11-28 09:23:40.85	38.7	141.796	76.3	215.94	2.8	9.77
29	2019-11-30 00:45:28.52	39.708	142.131	52.44	342.91	2.5	11.39
30	2019-11-30 01:34:14.16	39.759	141.838	68.98	324.04	2.6	10.45
31	2019-11-30 14:35:20.34	38.312	142.11	106.58	189.49	3	10.35
32	2019-12-01 06:24:29.28	40.196	142.21	104.76	355.31	2.7	11.35
33	2019-12-01 17:41:29.13	37.563	142.096	189.38	185.76	3.7	9.06
34	2019-12-01 18:08:22.39	38.49	142.274	85.41	182.14	3.5	16.56
35	2019-12-01 23:41:06.86	38.835	141.623	75.72	231.99	2.3	11.56